Monthly Notices of the Royal Astronomical Society
Open Access from January 2024
Discover more
Advertisement

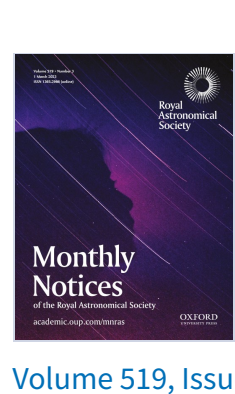

Volume 519, Issue 3
March 2023

Article Contents

ABSTRACT
1 INTRODUCTION
2 METHODOLOGY
3 ANALYTIC EXPECTATIONS
4 RESULTS
5 DISCUSSION
6 CONCLUSIONS
ACKNOWLEDGEMENTS
DATA AVAILABILITY
Footnotes
REFERENCES
APPENDIX A: COMPLETE SCATTER PLOTS OF POLARIZATION SPECTRAL INDICES
APPENDIX B: TESTS OF THE σ_{cut} PARAMETER

< Previous Next >

JOURNAL ARTICLE

Probing plasma physics with spectral index maps of accreting black holes on event horizon scales

Angelo Ricarte, Charles Gammie, Ramesh Narayan, Ben S Prather

Monthly Notices of the Royal Astronomical Society, Volume 519, Issue 3, March 2023, Pages 4203–4220, https://doi.org/10.1093/mnras/stac3796
Published: 26 December 2022 **Article history ▾**

PDF Split View Cite Permissions Share ▾

ABSTRACT

The *Event Horizon Telescope* (*EHT*) collaboration has produced the first resolved images of the supermassive black holes at the centre of our galaxy and at the centre of the elliptical galaxy M87. As both technology and analysis pipelines improve, it will soon become possible to produce spectral index maps of black hole accretion flows on event horizon scales. In this work, we predict spectral index maps of both M87* and Sgr A* by applying the general relativistic radiative transfer (GRRT) code IPOLE to a suite of general relativistic magnetohydrodynamic (GRMHD) simulations. We analytically show that the spectral index increases with increasing magnetic field strength, electron temperature, and optical depth. Consequently, spectral index maps grow more negative with increasing radius in almost all models, since all of these quantities tend to be maximized near the event horizon. Additionally, photon ring geodesics exhibit more positive spectral indices, since they sample the innermost regions of the accretion flow with the most extreme plasma conditions. Spectral index maps are sensitive to highly uncertain plasma heating prescriptions (the electron temperature and distribution function). However, if our understanding of these aspects of plasma physics can be tightened, even the spatially unresolved spectral index around 230 GHz can be used to discriminate between models. In particular, Standard and Normal Evolution (SANE) flows tend to exhibit more negative spectral indices than Magnetically Arrested Disc (MAD) flows due to differences in the characteristic magnetic field strength and temperature of emitting plasma.

Keywords: accretion, accretion discs, black hole physics, (*magnetohydrodynamics*) MHD, galaxies: individual (M87)
Issue Section: Article

1 INTRODUCTION

Every massive galaxy is believed to host a supermassive black hole (supermassive BH; SMBH) at its centre that, when supplied with gas to accrete, can shine and impart energy into its host galaxy as an active galactic nucleus (AGN) (Kormendy & Richstone 1995; Kormendy & Ho 2013). 'AGN feedback' in the form of radiation, winds, and/or jets is believed to be essential for regulating gas cooling in massive galaxies and is therefore a critical piece of galaxy evolution modelling (e.g. Croton et al. 2006; Heckman & Best 2014). Yet at present, the details of both accretion and feedback processes are poorly understood, motivating in-depth studies of the central engines of AGN.

In the past few years, the *Event Horizon Telescope* (*EHT*) has produced the first resolved images of SMBHs, ushering in a new era of spatially resolved accretion physics on event horizon scales. These include the SMBH at the centre of the M87 galaxy, henceforth M87* (Event Horizon Telescope Collaboration 2019a, b, c, d, e, f; 2021a, b), as well as the SMBH at the centre of our own galaxy, Sagittarius A* or Sgr A* (Akiyama et al. 2022a, b, c, d, e, f). Each is believed to be enveloped in a radiatively inefficient accretion flow (RIAF), a hot, geometrically thick, and optically thin accretion disc with a low Eddington ratio (Narayan & Yi 1994, 1995; Abramowicz et al. 1995; Narayan, Igumenshchev & Abramowicz 2000; Quataert & Gruzinov 2000; Yuan & Narayan 2014). For these systems, two of the most interesting parameters to constrain observationally are its spin and magnetic field state. The spin of a SMBH can be tapped to power jets (Blandford & Znajek 1977), and its cosmic evolution is sensitive to uncertain SMBH accretion and dynamics over billions of years (e.g. King, Pringle & Hofmann 2008; Volonteri et al. 2013). The magnetic field state of the accretion flow, whether a 'Magnetically Arrested Disc' (MAD) or 'Standard and Normal Evolution' (SANE; as discussed further in Section 2.1) describes whether or not the magnetic field is ordered and strong enough to affect the plasma dynamics. EHT imaging with resolved polarimetry, combined with other multiwavelength constraints, currently favour a MAD model with non-zero spin for M87* (Event Horizon Telescope Collaboration 2019e, 2021b). For Sgr A*, a promising cluster of relatively face-on, spinning MAD models passes most observational constraints (Akiyama et al. 2022e), and a full polarimetric analysis is underway.

The EHT aims to continue monitoring these sources while improving its capabilities by adding sites, improving bandwidth and recording speed, and enabling observations at other frequencies such as 86 and 345 GHz (Doeleman et al. 2019; Raymond et al. 2021). Continued monitoring alone is likely to constrain models based on time variability, and structural variability on event horizon scales has already been detected in EHT and 'proto-EHT' data (Wielgus et al. 2020). In addition to simply increasing the signal to noise, expanding the observed bandwidth can enable both total intensity and polarimetry studies in the frequency domain. Resolved rotation measure maps may reveal turbulent and non-uniform magnetic field structures that are predicted in simulations (Ricarte et al. 2020). It will also be possible to produce resolved spectral index maps on event horizon scales, which is the subject of this work. The spectral index of an emitting plasma, which we will denote as $\alpha \equiv \mathrm{d}\log I/\mathrm{d}\log \nu$, where I is the intensity and ν is the wavelength, is sensitive to its underlying magnetic field, its optical depth, and its electron energy distribution (e.g. Rybicki & Lightman 1986), all of which vary substantially in our models.

We focus our study on 230 GHz, the primary observing frequency of the EHT. As observed by the Atacama Large Millimeter Array (ALMA), Sgr A* exhibits $\alpha = 0.0 \pm 0.1$ at approximately this frequency (Goddi et al. 2021; Wielgus et al. 2022), with a more negative spectral index of $\alpha \approx -0.3$ between 230 and 870 GHz (Bower et al. 2019). For the core of M87, VLBI observations determined $\alpha \approx -0.4$ between 15 and 129 GHz, although the true spectral index may be nearer to 0 and steepened due to changes in (u,v) coverage (Kim et al. 2018). Meanwhile, $\alpha \approx -1.1$ was observed at 230 GHz using the Atacama Large Millimeter Array (ALMA) alone, but this measurement includes larger scale jet emission which probably drives the spectral index downwards (Goddi et al. 2021). Interpreting these significantly different spectral indices for M87 is complicated by the existence of extended emission that is resolved out by the EHT, as well as differences in (u,v) coverage, as discussed in appendix A of Kim et al. (2018).

In this work, we perform an exhaustive study of the spectral index on event horizon scales both analytically and using ray-traced general relativistic magnetohydrodynamics (GRMHD) simulations. In Section 2, we describe the GRMHD and ray-tracing calculations upon which most of this work is based. In Section 3, we briefly explore analytic expectations of the spectral index for a uniform slab of plasma. In Section 4, we discuss the main results of our simulated images, which include both spatially resolved spectral index maps and spatially unresolved spectral indices. We discuss further implications of our results in Section 5, then summarize our conclusions in Section 6.

2 METHODOLOGY

2.1 GRMHD

As our starting point, we consider 0 GRMHD simulations, first presented in Akiyama et al. (2022e). The simulations considered were run with the GRMHD code KHARMA (Prather et al. in preparation; Prather et al. 2021). The 0 GRMHD models cover two types of accretion states, MAD and SANE, around BHs with five different dimensionless spin parameters $a_\bullet \in \{-0.94, -0.5, 0, 0.5, 0.94\}$. MAD models accumulate strong and ordered magnetic fields that are powerful enough to affect disc dynamics (Bisnovatyi-Kogan & Ruzmaikin 1974; Igumenshchev, Narayan & Abramowicz 2003; Narayan, Igumenshchev & Abramowicz 2003; Chael, Narayan & Johnson 2019), while SANE models have dynamically weaker and more turbulent magnetic fields (Narayan et al. 2012; Sądowski et al. 2013; Ryan et al. 2018).

All models are performed at a resolution of 288 × 128 × 128 zones in r, θ, and ϕ, directions respectively, on a domain of radius $1000\,GM_\bullet/c^2$. The simulations in this work use the formulae and 'funky' MKS coordinate system and grid sizing outlined in Wong et al. (2022). Simulations are performed using RK2 time-stepping and WENO5 spatial reconstruction, with code details as outlined in Prather et al. (2021). Plasma is initialized in a Fishbone & Moncrief (1976) equilibrium torus solution, magnetized proportionally to density in SANEs and to both the density and the cube of radius in MADs. MADs are initialized with a torus with an inner boundary at $20\,GM_\bullet/c^2$ and a pressure maximum at $40\,GM_\bullet/c^2$, while SANEs are initialized with a torus with an inner boundary at $10\,GM_\bullet/c^2$ and a pressure maximum at $20\,GM_\bullet/c^2$. Magnetic flux is initialized and normalized as described in Wong et al. (2022), equations (33) and (34). All models are run to a final time of $3 \times 10^4\,GM_\bullet/c^3$, where G is the gravitational constant, $M_\bullet$ is the black hole mass, and c is the speed of light. To reduce the number of images needed for this study but still obtain some sense of the time variability, we image only eleven snapshots from each model, spaced evenly between $2.5 \times 10^4\,GM_\bullet/c^3$ and $3.0 \times 10^4\,GM_\bullet/c^3$. Since ideal GRMHD simulations are scale-free, we are able to use the same simulations to produce images of both M87* and Sgr A*.

2.2 GRRT

We use the code IPOLE to perform General Relativistic Ray Tracing (GRRT) calculations on the GRMHD outputs (Mościbrodzka & Gammie 2018). At this step, we specify the BH mass, its distance, the mass units of the plasma, and parameters related to electron heating. For M87*, we assume a BH mass of $6.2 \times 10^9\,\mathrm{M}_\odot$ and a distance of 16.9 Mpc from stellar dynamics (Gebhardt et al. 2011), for consistency with Event Horizon Telescope Collaboration (2019e, 2021b). For Sgr A*, we assume a BH mass of $4.14 \times 10^6\,\mathrm{M}_\odot$ and a distance of 8.123 kpc from stellar orbit studies (Boehle et al. 2016). GRMHD simulations are invariant under the transformation $\rho \rightarrow \mathcal{M}\rho$ and $B \rightarrow \sqrt{\mathcal{M}}B$, where ρ is the mass density, B is the magnetic field strength, and $\mathcal{M}$ is a scalar. Thus, we fit $\mathcal{M}$ such that at 228 GHz models of M87* maintain an average flux of 0.5 Jy and models of Sgr A* maintain an average flux of 2.4 Jy (Goddi et al. 2021). For a given model, this fixes the accretion rate, which is not a free parameter in our work.

The diffuse plasma accreting onto Sgr A* and M87* have low enough densities such that the mean free path is much larger than the size of the system. As a result, ions and electrons are not believed to achieve thermal equilibrium with each other (Shapiro, Lightman & Eardley 1976; Rees et al. 1982; Narayan, Yi & Mahadevan 1995). Models of electron heating predict that electrons are heated less efficiently than ions, and therefore acquire lower temperatures. The temperature ratio depends on the plasma $\beta \equiv P_{\mathrm{gas}}/P_{\mathrm{mag}}$, the ratio of the gas to magnetic pressure. More equal rates of heating are obtained when $\beta \rightarrow 0$, while the ions acquire more of the heating when $\beta > 1$ (Howes 2010; Chael et al. 2019; Kawazura, Barnes & Schekochihin 2019; Rowan, Sironi & Narayan 2019; Mizuno et al. 2021). To account for this effect, we prescribe the electron temperature relative to the ion temperature (which originates from the GRMHD) via the widely used Mościbrodzka, Falcke & Shiokawa (2016) prescription,

$$\frac{T_i}{T_e} = R_{\mathrm{high}}\frac{\beta^2}{1+\beta^2} + R_{\mathrm{low}}\frac{1}{1+\beta^2}. \tag{1}$$

For this study, we consider $R_{\mathrm{high}} \in \{1, 10, 40, 160\}$ but fix $R_{\mathrm{low}} = 1$.

While most GRRT in the literature is performed assuming a thermal electron distribution function (eDF), the spectral energy distributions of Sgr A* and M87* favour a non-thermal component. Higher energy electron populations than available in a thermal eDF are believed to be important for reproducing the flux in the near-infrared and can increase the sizes of images (Özel, Psaltis & Narayan 2000; Mao, Dexter & Quataert 2017; Davelaar et al. 2018).

For our non-thermal eDF models, we explore three different 'kappa' distributions, which have a thermal core and a power law tail that extends to high energies with slope $\mathrm{d}\log n/\mathrm{d}\log\gamma = \varkappa - 1$ (Vasyliunas 1968). This distribution finds its origins in fits to the observed solar wind (Decker & Krimigis 2003; Pierrard & Lazar 2010), and is naturally produced in simulations of particle acceleration in an accretion disc (Kunz, Stone & Quataert 2016). The relativistic kappa distribution is given by

$$\frac{\mathrm{d}n_e}{\mathrm{d}\gamma\,\mathrm{d}\cos\xi\,\mathrm{d}\phi} = \frac{N}{4\pi}\gamma(\gamma^2-1)^{1/2}\left(1+\frac{\gamma-1}{\kappa w}\right)^{-(\kappa+1)}, \tag{2}$$

where N is the overall normalization, γ is the Lorentz factor, ξ is the pitch angle, ϕ is the gyrophase, and $\varkappa$ and w are dimensionless free parameters (Xiao 2006). As $\varkappa \rightarrow \infty$, the kappa distribution becomes a thermal distribution. For our study, we explore three global values for $\varkappa \in \{3.5, 5.0, 7.0\}$ that do not change within the simulated region. Meanwhile, we scale the width w with the electron temperature in each cell via

$$w = \Theta_e\frac{\kappa-3}{\kappa}, \tag{3}$$

where Θ_e is the electron temperature in units of the electron rest mass. This prescription preserves the total amount of energy in the distribution with respect to thermal (as long as $\varkappa < 3$).

We adopt the polarized emissivities j_ν and absorptivities α_ν for a kappa distribution from SYMPHONY (Pandya et al. 2016). SYMPHONY provides fitting formulae for j_ν and α_ν as a function of magnetic field, electron temperature, and electron number density. Meanwhile, our radiative transfer coefficients for thermal distributions originate from Dexter (2016). We set all radiative transfer coefficients to 0 in highly magnetized regions ($\sigma \equiv B^2/\rho > \sigma_{\mathrm{cut}} = 1$), where numerical floors can result in the artificial injection of material. We do not expect that this cut has strong qualitative effects on our results, although it may be more impactful in models where $\varkappa$ scales with σ (e.g. Davelaar et al. 2018; Fromm et al. 2022; Scepi, Dexter & Begelman 2022). The effect of this choice is briefly explored in Appendix B.

In summary, we create images for two sources (M87*, Sgr A*), two magnetic field states (MAD, SANE), five spins, eleven snapshots, four values of R_{high}, four eDF models, and for Sgr A* three inclinations. For each of these models, we produce images at four frequencies, $\nu \in \{214.1, 228.1\}$ GHz for Sgr A* and $\nu \in \{214.1, 228.1, 340.0, 350.0\}$ GHz for M87*, where the first two values are specifically chosen to emulate EHT 2018 observations. This results in a library containing a total of 17 600 images. These are created with an angular resolution of 0.5 μas, and a field of view of 240 μas for M87* and 300 μas for Sgr A*. These are larger fields of view than typically adopted, since images with non-thermal electrons tend to be larger than thermal ones (Özel et al. 2000; Mao et al. 2017; Davelaar et al. 2018). For all images, an outer integration radius of $50\,GM_\bullet/c^2$ is used for the radiative transfer.

Throughout, we define the spectral index $\alpha \equiv \mathrm{d}\log I_\nu/\mathrm{d}\log\nu$. When considering an image's spectral index, α_{net} is the spectral index one would infer from a spatially unresolved measurement.

3 ANALYTIC EXPECTATIONS

To interpret the results of our GRRT calculations, let us first explore analytic calculations for a uniform slab of material with a magnetic field strength $|B|$, electron temperature in units of rest mass energy Θ_e, and thickness s. Throughout, we also assume that the magnetic field is oriented perpendicular to the photon wave-vector. From these properties, we can compute the emissivity $j_\nu(B, \Theta_e)$ and absorptivity $\alpha_\nu(B, \Theta_e)$[1] using the fitting functions provided in Pandya et al. (2016). With this simple setup, the radiative transfer equation reduces to

$$I_\nu = \frac{j_\nu}{\alpha_\nu}\left(1-e^{-\tau_\nu}\right),\ \tau_\nu \equiv \alpha_\nu s, \tag{4}$$

where I_ν is the observed intensity, and τ_ν is the optical depth.

3.0.1 Optically thin

In the optically thin limit ($\tau_\nu \rightarrow 0$), equation (4) reduces to $I_\nu = j_\nu s$. Thus, the spectral index depends only on the emissivity coefficient j_ν, via $\alpha = \mathrm{d}\log j_\nu/\mathrm{d}\log\nu$. In Fig. 1, we plot $\alpha(\nu)$ in the optically thin limit for several combinations of magnetic field strength $|B|$ and electron temperature Θ_e. Thermal models are plotted with solid lines, while $\varkappa = 5.0$ models are plotted with dotted lines. A dashed black line demarcates 230 GHz, the primary observing frequency of the EHT and the focus of this study.

Figure 1.

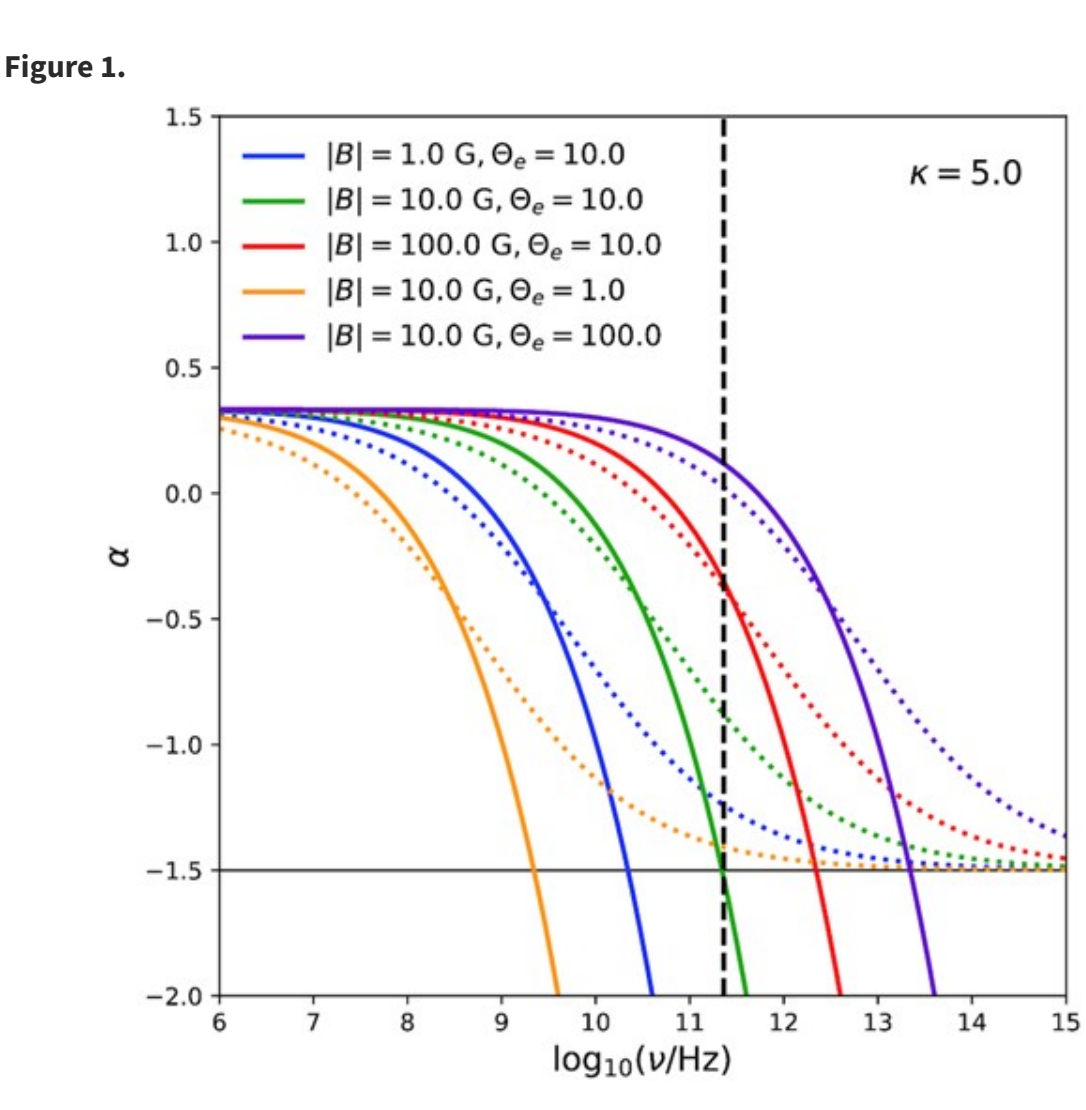

Open in new tab Download slide

Spectral index as a function of frequency in the optically thin limit for a uniform slab of plasma. Models with $\kappa = 5$ are plotted with dotted lines, while thermal models are plotted with solid lines. Different colours correspond to different combinations of magnetic field strength $|B|$ and electron temperature Θ_e. A black vertical dashed line marks 230 GHz, the primary observing frequency of the EHT, and the focus of this study. In the optically thin and low frequency limit, both classes of models approach $\alpha = 1/3$. Models turn over at a critical frequency $\nu_{\mathrm{crit}} \propto B\Theta_e^2$. In the optically thin and high frequency limit, kappa models asymptote to a value of $\alpha_{\mathrm{min}} = -(\kappa - 2)/2$, plotted with a horizontal black line, while thermal models diverge to $-\infty$.

Plasmas with both thermal and kappa eDFs have critical frequencies $\nu_{\mathrm{crit}} \propto \Theta_e^2 B$ where these curves turn over (see Pandya et al. 2016, for details). At fixed observing frequency, optically thin plasmas with higher temperatures or magnetic field strengths exhibit more positive spectral indices, up to a maximum value of $\alpha = 1/3$ for either class of model. On the other hand, as $\nu/\nu_{\mathrm{crit}} \rightarrow \infty$, α diverges to $-\infty$ for thermal models, but asymptotes to $\alpha_{\mathrm{min}} = -(\varkappa - 2)/2$ for kappa models, which we mark with a thin black horizontal line. This asymptote is identical to that of a power law eDF described by $n(\gamma) \propto \gamma^{-p}$ with $p = \varkappa - 1$. Any model with a uniform value of kappa throughout the simulation domain cannot exhibit a spectral index $\alpha < \alpha_{\mathrm{min}}$.

3.0.2 Optically thick

Finite optical depth always causes the spectral index of a uniform slab of material to increase. In Figs 2 and 3, we plot the spectral index as a function of optical depth, varying the magnetic field strength and the frequency respectively. We fix $\Theta_e = 10$ and $\nu = 230$ GHz in Fig. 2 and fix $\Theta_e = 10$ and $|B| = 10$ G in Fig. 3. In the optically thick limit ($\tau_\nu \rightarrow \infty$), equation (4) reduces to $I_\nu = j_\nu/\alpha_\nu$, and consequently $\alpha = \mathrm{d}\log j_\nu/\mathrm{d}\log\nu - \mathrm{d}\log\alpha_\nu/\mathrm{d}\log\nu$. For a thermal distribution, $\alpha \rightarrow 2$ (the Rayleigh-Jeans law), whereas for a kappa distribution the spectral index approaches a value between 2 and 5/2 depending on the plasma details, $\alpha_{\mathrm{max}}(\varkappa, \nu, B, \Theta_e) \in (2, 2.5)$.

Figure 2.

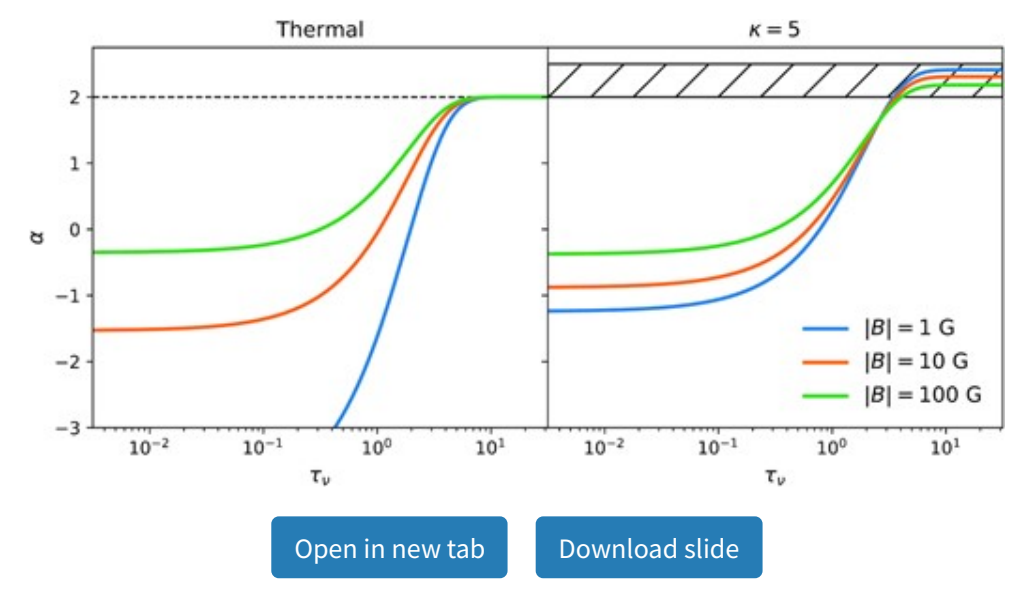

Open in new tab Download slide

Spectral indices for a uniform slab of plasma as a function of optical depth for different magnetic field strengths with fixed $\Theta_e = 10$ and $\nu = 230$ GHz. Increasing the optical depth increases α from the optically thin limit (Fig. 1) up to $\alpha_{\mathrm{max}} = 2$ for thermal models (left; dashed black line), or $\alpha_{\mathrm{max}}(\kappa, \nu, B, \Theta_e) \in (2, 2.5)$ for a kappa model (right; hashed region).

Figure 3.

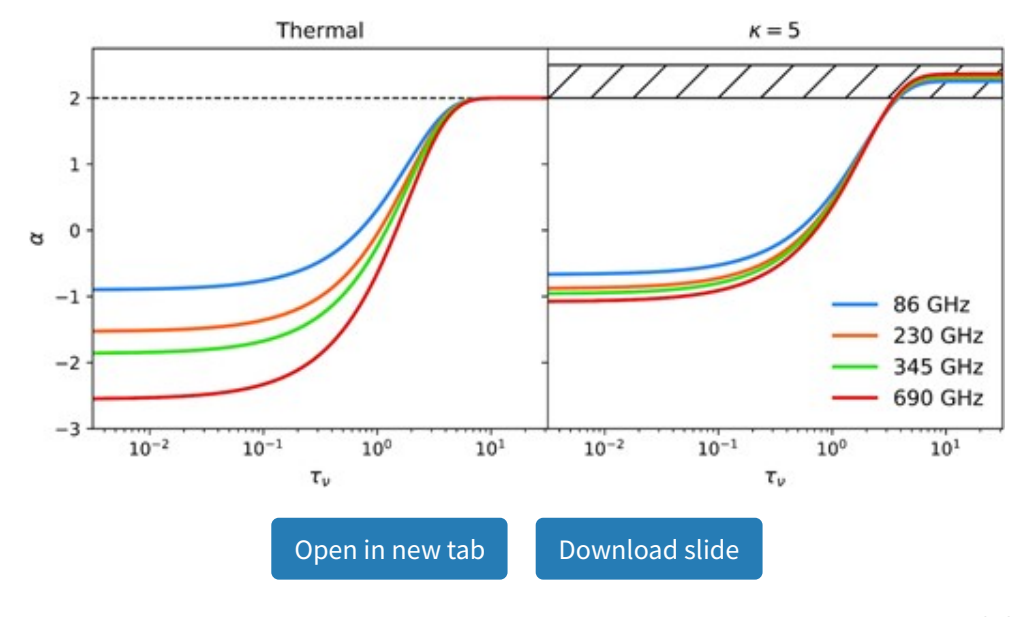

Open in new tab Download slide

As Fig. 2, but varying frequency instead of magnetic field strength. Here, we fix $\Theta_e = 10$ and $|B| = 10$ G. Higher frequencies result in more negative spectral indices for small τ_ν (see also Fig. 1), while the spectral index necessarily converges to similar values for large τ_ν. (Note that since τ_ν is frequency-dependent, a given τ_ν in this plot implies a different physical column density for each frequency curve.)

In summary, the spectral index of a uniform slab of material with either a thermal or kappa eDF depends on three parameters: its magnetic field strength $|B|$, its electron temperature Θ_e, and its optical depth τ_ν. Synchrotron emitting plasma has a critical frequency $\nu_{\mathrm{crit}} \propto \Theta_e^2 B$, so increasing either Θ_e or B will increase α in the optically thin limit up to a maximum value of 1/3. In the optically thin limit, $\alpha \in (-(\varkappa - 2)/2, 1/3)$ for kappa eDFs, while $\alpha \in (-\infty, 1/3)$ for thermal eDFs. Optical depth can increase α to $\alpha_{\mathrm{max}} = 2$ for a thermal eDF, or $\alpha_{\mathrm{max}}(\varkappa, \nu, B, \Theta_e) \in (2, 2.5)$ for a kappa eDF.

4 RESULTS

4.1 Resolved spectral index maps: a first glance

In Fig. 4, in the first row, we first introduce an example model's intensity map, spectral index map,[2] and an analytic estimate of the spectral index map based on emission-weighted physical quantities in each pixel. This model corresponds to a snapshot of the Sgr A* MAD $a_\bullet = 0$ $R_{\mathrm{high}} = 40$ $\varkappa = 5$ $i = 50°$ model, which has $\alpha_{\mathrm{net}} = -0.26$. The spectral index becomes more negative as one moves farther from the centre of the image. The photon ring also stands out, exhibiting a more positive spectral index than its surroundings.

Figure 4.

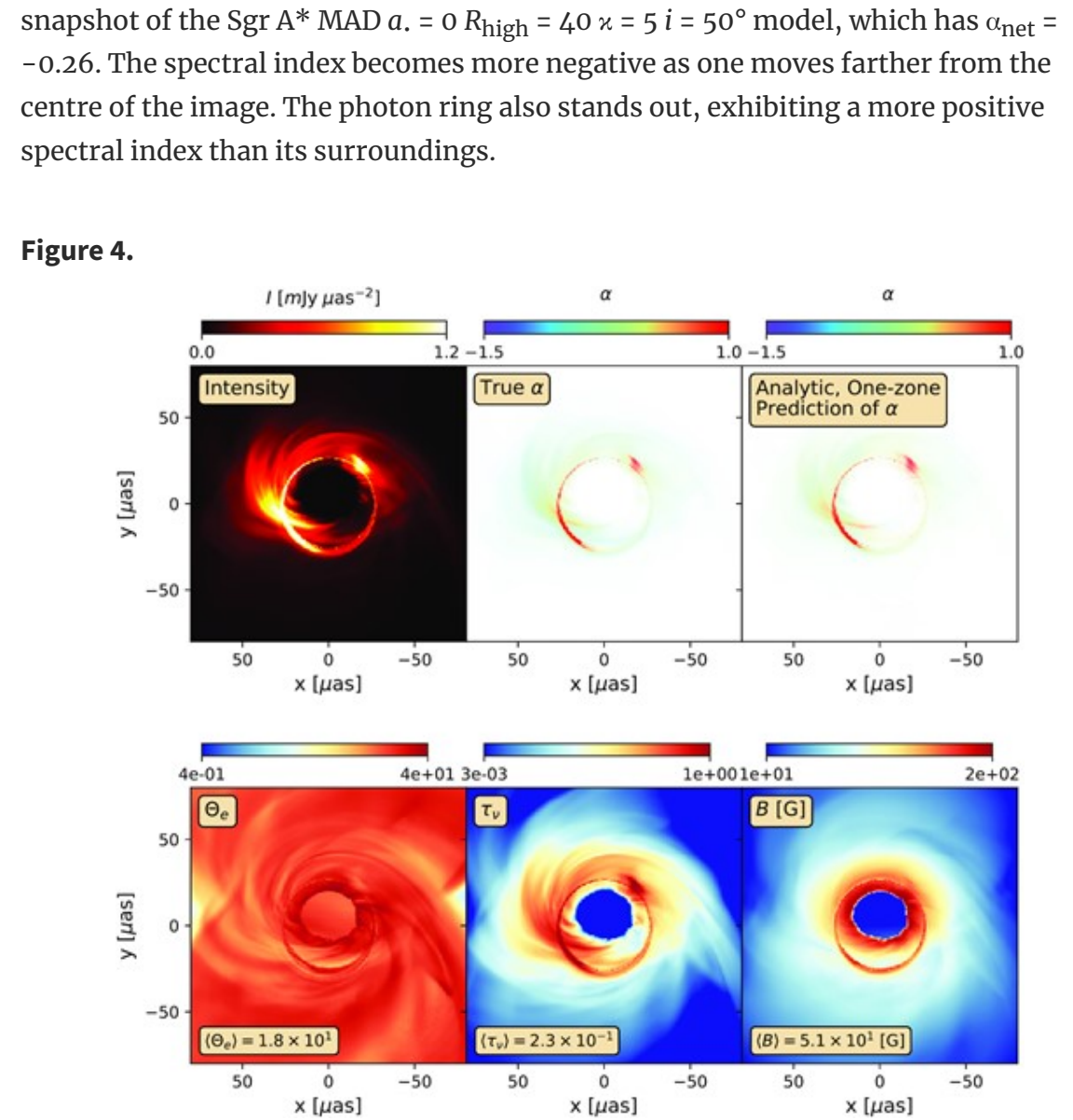

Open in new tab Download slide

Top: For one model of Sgr A*, an intensity map, spectral index map, and predicted spectral index map from characteristic physical quantities in each pixel between 214.1 and 228.1 GHz. The results shown correspond to a snapshot of the MAD $a_\bullet = 0$ $R_{\mathrm{high}} = 40$ $\kappa = 5$ $i = 50°$ model, which exhibits $\alpha_{\mathrm{net}} = -0.26$. *Bottom:* Pixel-wise emissivity-weighted average temperatures, optical depths, and magnetic field strengths along each geodesic. Image-averaged intensity-weighted quantities are computed and written on the bottom of each panel. These quantities are used to analytically predict the spatially resolved spectral index map in the top right-hand panel, which agrees excellently with the true spectral index map computed from full ray-tracing with IPOLE at two frequencies shown in the top middle panel. Two salient features of the spectral index map can be explained by examining these physical parameters. First, the radial decline in α can be explained by a corresponding decline in the magnetic field strength and optical depth. Secondly, the photon ring shows up clearly on the spectral index map. These geodesics have large optical depths due to their longer path lengths, and also because they plunge into the innermost regions of the accretion flow, with the largest magnetic field strengths.

By computing emission-weighted physical quantities in each pixel, shown in the second row, we can understand these features. Here, for a given physical quantity $\xi(\lambda)$, we assign a single emission-weighted value to each pixel $\bar{\xi} = \int\xi(\lambda)j_\nu(\lambda)\mathrm{d}\lambda/\int j_\nu(\lambda)\mathrm{d}\lambda$, where λ is the affine parameter describing the geodesic. Written on the bottom of each panel, we then assign a single characteristic value to each image by performing an intensity-weighted sum across all pixels, $\langle\xi\rangle = \int\bar{\xi}I(x,y)\mathrm{d}x\mathrm{d}y/\int I(x,y)\mathrm{d}x\mathrm{d}y$. Given characteristic values of Θ_e, τ_ν, and B in each pixel, we can then use the analysis developed in Section 3 to predict α in each pixel. Comparing this analytic, one-zone prediction to the true α computed by performing full ray-tracing with IPOLE at two different frequencies, we find exceptional agreement.

Thus, we can explain the two main features in the spectral index map, its radial decline and spike at the photon ring. Recall that α increases if $\nu_{\mathrm{crit}} \propto B\Theta_e^2$ increases. The radial decline in α can be explained by a similar decline in the characterstic magnetic field strength in the emitting region. In addition, α also increases if τ_ν increases, and we see that τ_ν indeed also decreases with radius in this image. Finally, both τ_ν and B are largest in the photon ring, whose geodesics have the longest path lengths in the emitting region, hence the largest τ_ν, and also probe the innermost regions of the accretion flow.

In Fig. 5, we repeat this analysis for a SANE snapshot of Sgr A* which has otherwise the same parameters (Sgr A* SANE $a_\bullet = 0$ $R_{\mathrm{high}} = 40$ $\varkappa = 5$ $i = 50°$). This model has a much lower value of $\alpha_{\mathrm{net}} = -0.97$ compared to the MAD snapshot's $\alpha_{\mathrm{net}} = -0.26$, which we will discuss as a generic feature distinguishing the two magnetic field states in Section 4.4. With each model's density and magnetic field self-consistently scaled to produce an average flux of 2.4 Jy, they actually exhibit similar values of $\langle\tau_\nu\rangle$ and $\langle B\rangle$. However, the SANE is colder than the MAD by an order of magnitude, resulting in the much lower α_{net}. The tendency for MADs to be hotter than SANEs is also reported in Akiyama et al. (2022e), who also find higher temperatures for larger and more prograde spins. Note that although the jet funnel is visible in the Θ_e map (oriented vertically in projection), these regions do not contribute noticeably to the intensity, which depends also on the density and magnetic field strength. We comment that these simulations have neglected radiative cooling, which may further reduce the temperature, and therefore also lower the spectral index.

Figure 5.

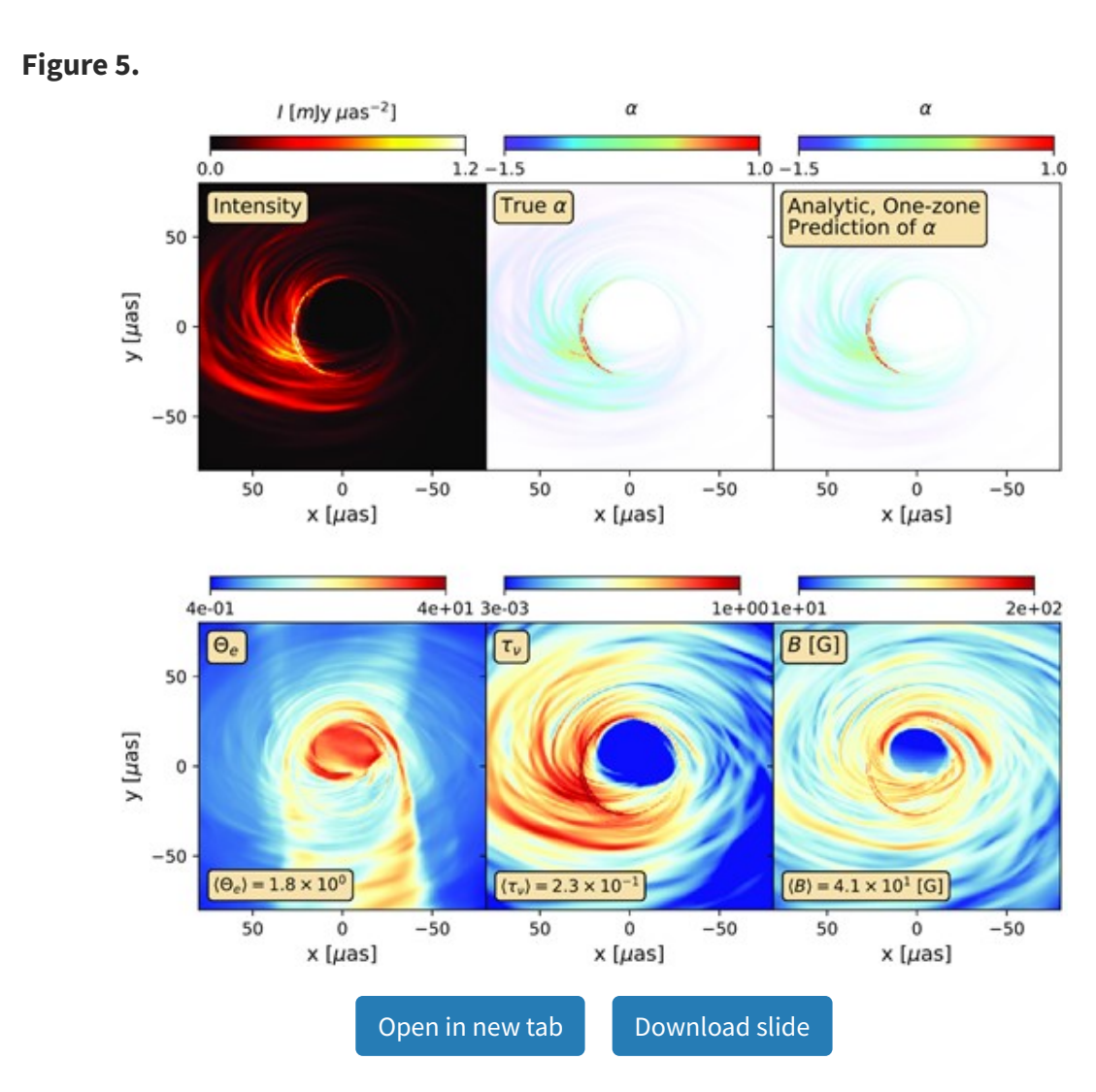

Open in new tab Download slide

As Fig. 4, but for the equivalent SANE snapshot (SANE $a_\bullet = 0$ $R_{\mathrm{high}} = 40$ $\kappa = 5$ $i = 50°$). Despite very similar optical depths and magnetic field strengths, the SANE model has a much more negative $\alpha_{\mathrm{net}} = -0.97$ compared to $\alpha_{\mathrm{net}} = -0.26$ for the MAD model. As illustrated by the bottom left-hand panels of these figures, this is due to the fact that the SANE disc is colder than the MAD disc by an order of magnitude.

4.2 Changing the electron distribution function

In Fig. 6, we explore how our images and their the spectral index maps behave with respect to our choices of source, eDF, and for Sgr A*, the inclination. The example chosen here is a SANE $a_\bullet = 0.94$ $R_{\mathrm{high}} = 40$ snapshot. The source and viewing angle of the models in each row are written in the left-most column, while the unresolved spectral index and characteristic optical depth are written at the bottom of each panel.

Figure 6.

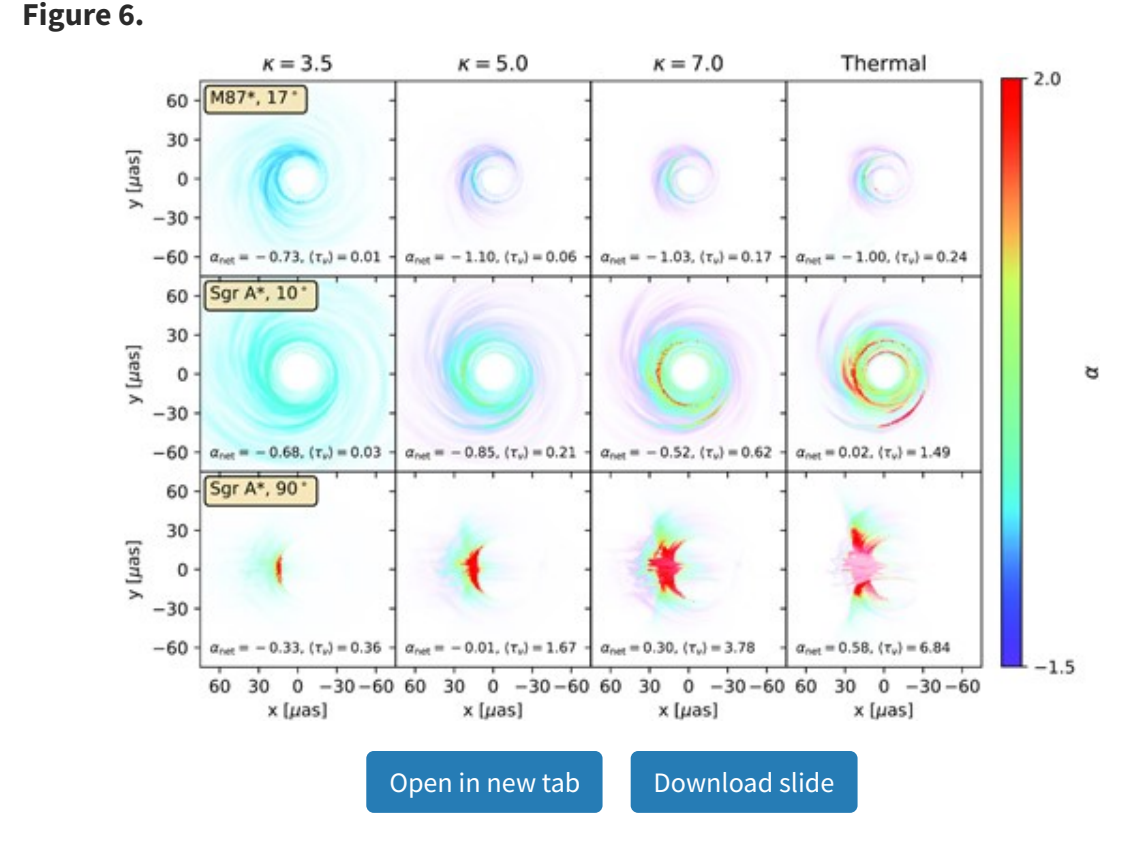

Open in new tab Download slide

Visualization of how the spectral index map (214.1–228.1 GHz) varies for a single snapshot as we change our choices of source, κ, and inclination angle. The addition of a non-thermal component produces a halo of diffuse emission that grows in prominence as κ decreases, consistent with previous studies (Özel et al. 2000; Mao et al. 2017). Models are more optically thick at larger inclinations and with smaller fractions of non-thermal electrons, therefore exhibiting more positive spectral indices. This particular SANE is significantly optically thick for $i = 90°$ and $\kappa \ge 5$, leading to positive spectral indices.

Recall that smaller values of $\varkappa$ correspond to a larger fraction of high-energy electrons, and that a thermal model corresponds to $\varkappa \rightarrow \infty$. Consistent with previous studies, the addition of a high-energy, non-thermal tail leads to a diffuse halo of emission which grows more prominent as $\varkappa$ decreases (Özel et al. 2000; Mao et al. 2017). Since we re-normalize the accretion rate to maintain a consistent average flux for each source, the addition of more non-thermal electrons (decreasing $\varkappa$) decreases the optical depth as the emitting region is spread out over a wider area. This in turn helps decrease the spectral index as $\varkappa$ decreases. This particular SANE model exhibits a strong dependence of α_{net} on the observing inclination, growing significantly optically thick for $i = 90°$ and $\varkappa \ge 5$, resulting in flat to positive α_{net}. We do not notice significant qualitative differences between our spectral index maps of M87* images and Sgr A* images, except that our Sgr A* images tend to be more optically thick and exhibit more positive spectral indices than our M87* images for the flux normalizations that we have adopted.

SANE model images have been shown to be more sensitive to electron temperature prescriptions (R_{high}) than MAD models (Event Horizon Telescope Collaboration 2019e), and the same appears to be true for the electron distribution function (eDF). In Fig. 7, we repeat this plot for a MAD $a_\bullet = -0.5$ $R_{\mathrm{high}} = 160$ model, a favoured combination of parameters for M87* from imaging and polarimetry analysis (Event Horizon Telescope Collaboration 2021b), and find much weaker variation. We generally find that MAD models are less sensitive to the choice of $\varkappa$ than SANEs.

Figure 7.

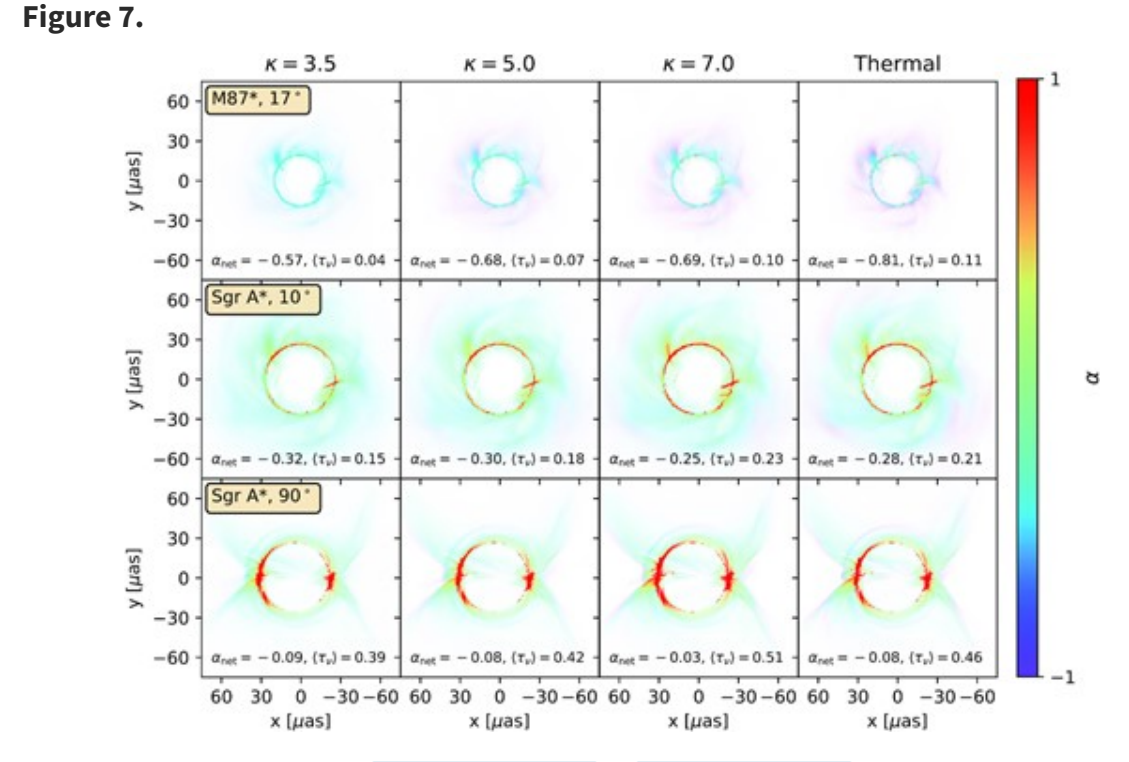

Open in new tab Download slide

As Fig. 7, but for a MAD $a_\bullet = -0.5$ $R_{\mathrm{high}} = 160$ model, a favourable combination of parameters for M87*

Monthly Notices of the Royal Astronomical Society
Open Access from January 2024
Discover more
Advertisement

CITATIONS VIEWS 132 ALTMETRIC 2
More metrics information

Email alerts
Article activity alert
Advance article alerts
New issue alert
In progress issue alert
Receive exclusive offers and updates from Oxford Academic

Recommended

Observational signatures of black hole accretion: rotating versus spherical flows with tilted magnetic fields
Jia 佳 瑟 et al., Monthly Notices of the Royal Astronomical Society, 2022

Using Machine Learning to Link Black Hole Accretion Flows with Spatially Resolved Polarimetric Observables
Richard Qiu et al., Monthly Notices of the Royal Astronomical Society, 2023

Scale-invariance of black-hole accretion: modelling emission from a black hole X-ray binary with relativistic accretion flow simulations
M Mościbrodzka, Monthly Notices of the Royal Astronomical Society, 2019

Analogue Black Holes in Reactive Molecules
Ren Zhang et al., Chinese Physics Letters, 2023

Self-assembled TiO2 hole-blocking layers for efficient perovskite solar cells
Zhongbao Que et al., International Journal of Minerals, Metallurgy and Materials, 2022

Quantum Oscillations in Noncentrosymmetric Weyl Semimetal SmAlSi
Weizheng Cao et al., Chinese Physics Letters, 2022

Powered by TREND MD

Astrophysics Data System
ADS Abstract

Citing articles via
Web of Science (2)
Google Scholar

Latest Most Read Most Cited
RR Lyrae from Binary Evolution: Abundant, Young and Metal-Rich
WISDOM Project - XVI. The link between circumnuclear molecular gas reservoirs and active galactic nucleus fuelling
Do ultra diffuse galaxies with rich globular clusters systems have overly massive halos?
Optimizing the gravitational tree algorithm for many-core processors
Wide post-common envelope binaries containing ultramassive white dwarfs: evidence for efficient envelope ejection in massive AGB stars

More from Oxford Academic
Astronomy and Astrophysics Physics
Science and Mathematics Books
Journals

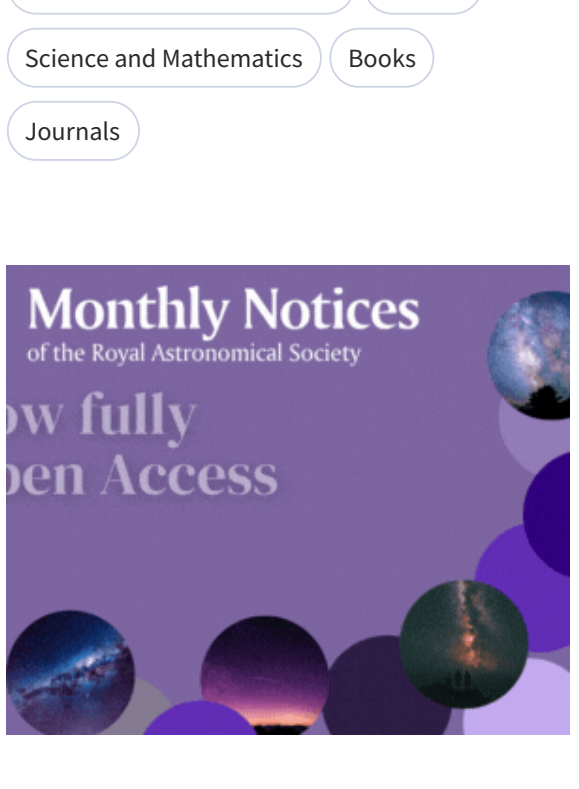
Monthly Notices of the Royal Astronomical Society
Now fully Open Access

(Event Horizon Telescope Collaboration 2021b). We broadly find MAD models to be less sensitive to the choice of κ than SANE models.

4.3 Resolved spectral index maps: a generic radial decline

A generic property of all resolved spectral index maps is that the spectral index grows more negative as radius increases. In Fig. 8, we plot average radial profiles of the spectral index between 214.1 and 228.1 GHz for each of the M87* models. For each model, we perform an intensity-weighted azimuthal average of the spectral index in each pixel, followed by a time-average. The top set of panels shows results for a thermal eDF, while the lower set of panels shows results for a $\varkappa = 5.0$ eDF. Note the different extent in the *y*-axis for the two sets of models. Curves transition from solid to dotted at the radius enclosing 95 per cent of the total flux.

Figure 8.

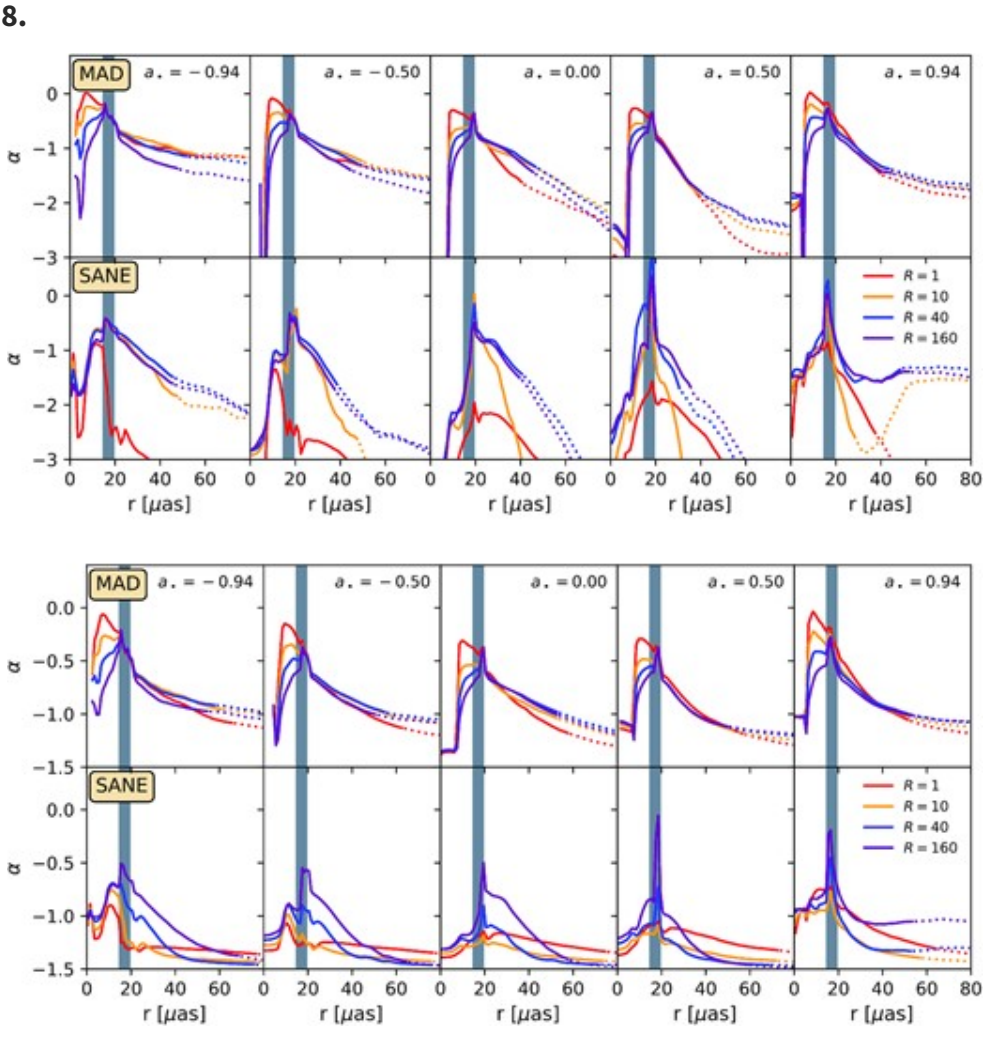

Open in new tab
Download slide

Azimuthally and time-averaged spectral index profiles (214.1–228.1 GHz) as a function of radius for a thermal eDF (*top*) and for a κ = 5 eDF (*bottom*) for M87* models. Note the difference in *y*-axis extent between the two eDF models. Different columns correspond to different spins, different rows correspond to different magnetic field states, and the colours encode different values of $R_{\rm high}$. The vertical grey band marks the radius of the photon ring, calculated analytically, which varies slightly with azimuth. The transition from solid to dotted curves marks the radius enclosing 95 per cent of the total emission in the image.

For most models, a spike in the spectral index occurs at the location of the photon ring, marked with a vertical grey band.[3] Interior to the photon ring, MAD models with larger $R_{\rm high}$ have more negative spectral indices, consistent with expectations as the electron temperature decreases. However, we caution that this region may be sensitive to our choice to zero radiative transfer coefficients within $\sigma > 1$ regions. Outside the photon ring, the spectral index universally falls off as radius increases. This matches general expectations that the image should become smaller as the frequency increases (e.g. Doeleman et al. 2008). Thermal models tend to fall off more rapidly than $\varkappa$ models, which are more likely to plateau at large radius. This is because in the optically thin limit, $\varkappa$ model spectral indices can never fall below $\alpha_{\rm min} = -(\varkappa - 2)/2$ (see Fig. 1). Consequently, the spectral index in optically thin regions in the image outskirts can place a lower limit on $\varkappa$.

While Fig. 8 assumes perfect resolution, the EHT currently only has a resolution of approximately 20 μas. In Fig. 9, we repeat the analysis done to create Fig. 8, but first blur each image with a Gaussian with a full width at half maximum of 20 μas. We find that the sharp photon ring feature is washed out, but the overall radial trends of these curves are preserved. In future EHT analyses, $d\alpha/dr$ may be useful for placing constraints on models. The shallowest gradients are exhibited by small $R_{\rm high}$ SANEs with a kappa eDF, which asymptote to $\alpha_{\rm min}$. The steepest gradients are exhibited by thermal SANEs, due to their low temperatures.

Figure 9.

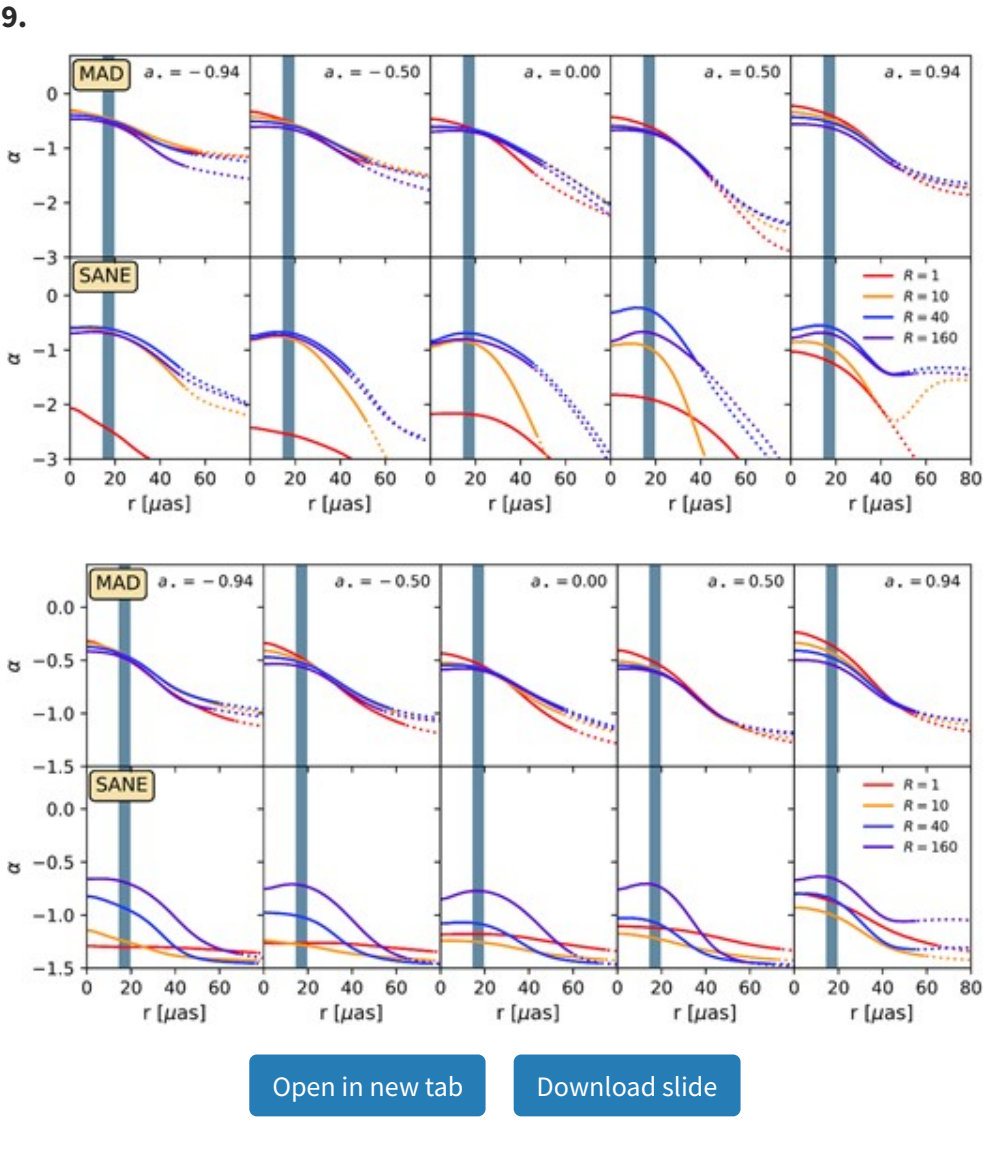

Open in new tab
Download slide

As Fig. 8, but each image is first convolved with a Gaussian with a full width at half-maximum of 20 μas. While the sharp photon ring feature is washed out, the overall radial trend is preserved. Future EHT analyses can use dα/d*r* to constrain models, for which we expect a negative value.

4.4 Unresolved spectral indices

Even lacking the spatial resolution of the EHT, the spatially unresolved spectral index, $\alpha_{\rm net}$, can discriminate models. The spectral index is sensitive to uncertain plasma parameters (Θ_e, eDF) as well as the magnetic field state (MAD vs SANE), but appears relatively insensitive to spin.

We plot $\alpha_{\rm net}$ as a function of optical depth for $\varkappa = 5$ models of M87* in Fig. 10. We focus on $\varkappa = 5$ for brevity, but note that the qualitative behaviour is similar for other eDFs, the main difference being the value of $\alpha_{\rm min}(\varkappa)$. In this plot, different colours encode different $R_{\rm high}$, different symbols encode different spins, and whether or not the symbol is filled encodes the magnetic field state, as indicated in the legend.

Figure 10.

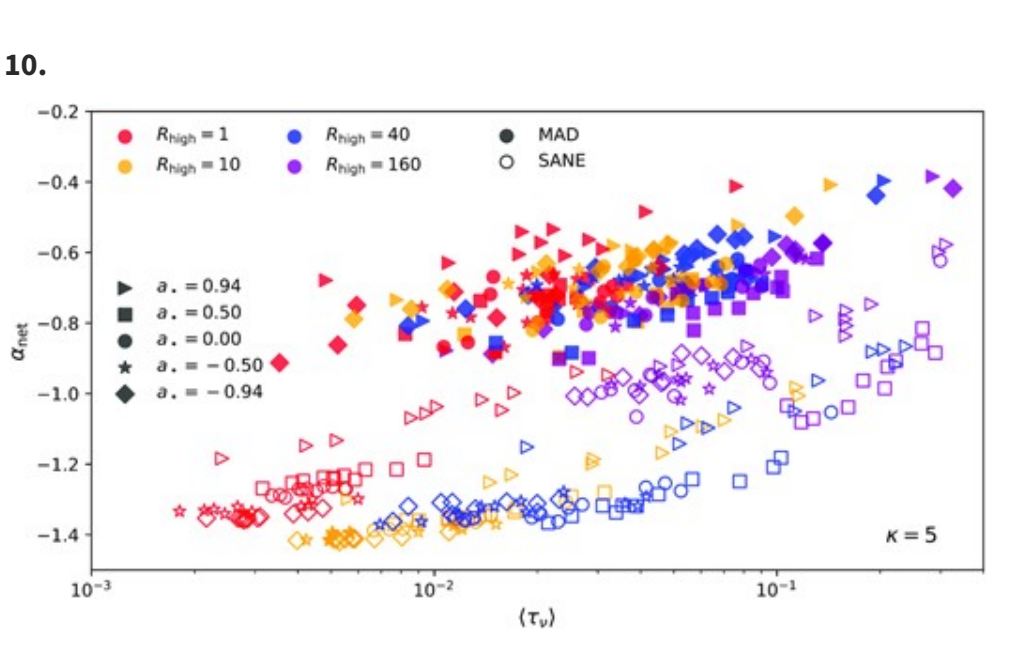

Open in new tab
Download slide

Unresolved spectral index ($\alpha_{\rm net}$, 214.1–228.1 GHz) versus optical depth $\langle\tau_\nu\rangle$ for M87* models with κ = 5. Different symbols correspond to different spin values, over which α exhibits no overall trend. Filled symbols correspond to MADs while open symbols correspond to SANEs, each of which occupy different regions of this parameter space. Although both classes of model span a similar range in optical depth, MAD models have more positive spectral indices than SANE models. Different colours correspond to different values of $R_{\rm high}$. For κ = 5, the spectral index approaches $\alpha_{\rm min} = -(\kappa - 2)/2 = -1.5$ in the optically thin limit, towards which the SANE models asymptote.

Our models span a wide range of both optical depth and spectral index despite all being normalized to produce the same average total intensity of 0.5 Jy. The most apparent trend is that while the MADs (filled circles) and SANEs (open circles) span the same range of optical depth, MADs exhibit more positive spectral indices than SANEs. This implies that MADs have larger values of $B\Theta_e^2$ in their emitting regions than SANEs. Recall that in Figs 4 and 5, we found that a difference in spectral index at similar optical depth was driven by an order of magnitude difference in Θ_e. Meanwhile, there is no obvious trend in $\alpha_{\rm net}$ as a function of spin, which we will show more clearly in Fig. 12. Finally, although there are trends in $\alpha_{\rm net}$ as a function of $R_{\rm high}$, these are more subtle and difficult to interpret, since the emitting region changes as $R_{\rm high}$ changes. We comment that for a fixed emitting region, one would analytically expect that increasing $R_{\rm high}$ should decrease $\alpha_{\rm net}$ at fixed $\langle\tau_\nu\rangle$, since Θ_e decreases with increasing $R_{\rm high}$, and the MAD models are consistent with this behaviour.

Figure 11.

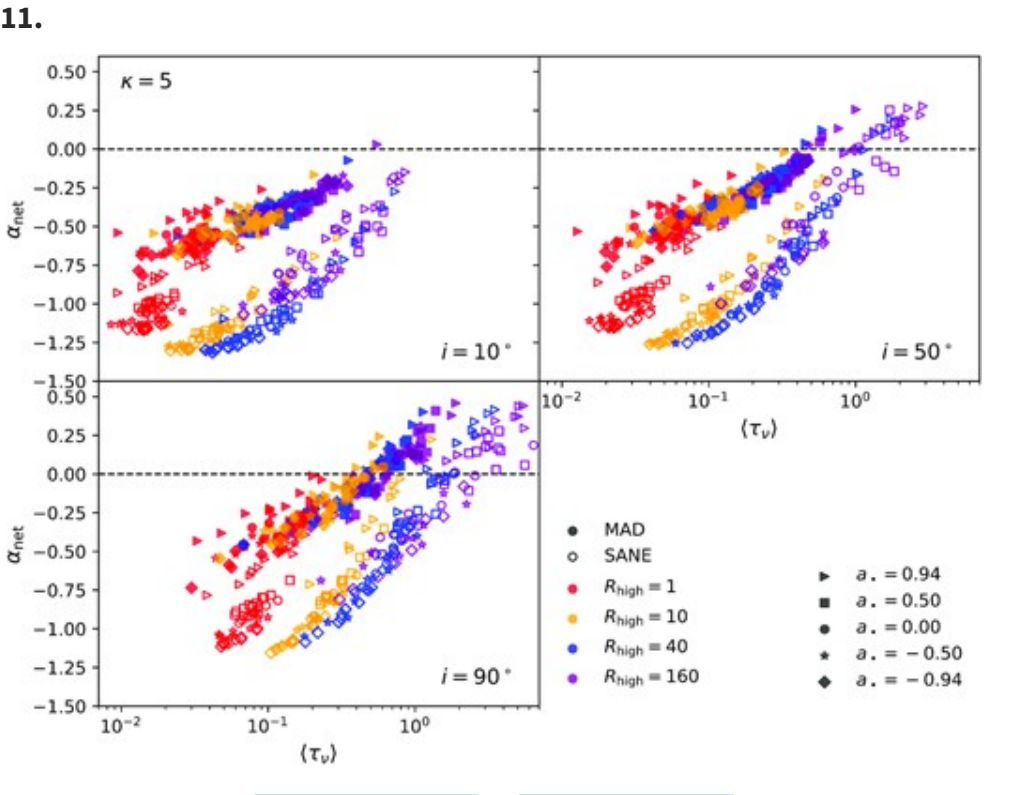

Open in new tab
Download slide

As Fig. 10, but for Sgr A* models with varying inclination. Behaviour is qualitatively similar for Sgr A* compared to M87*, but models tend slightly towards larger optical depths and more positive spectral indices. In addition, models are more optically thick and have higher spectral indices at larger inclinations.

Figure 12.

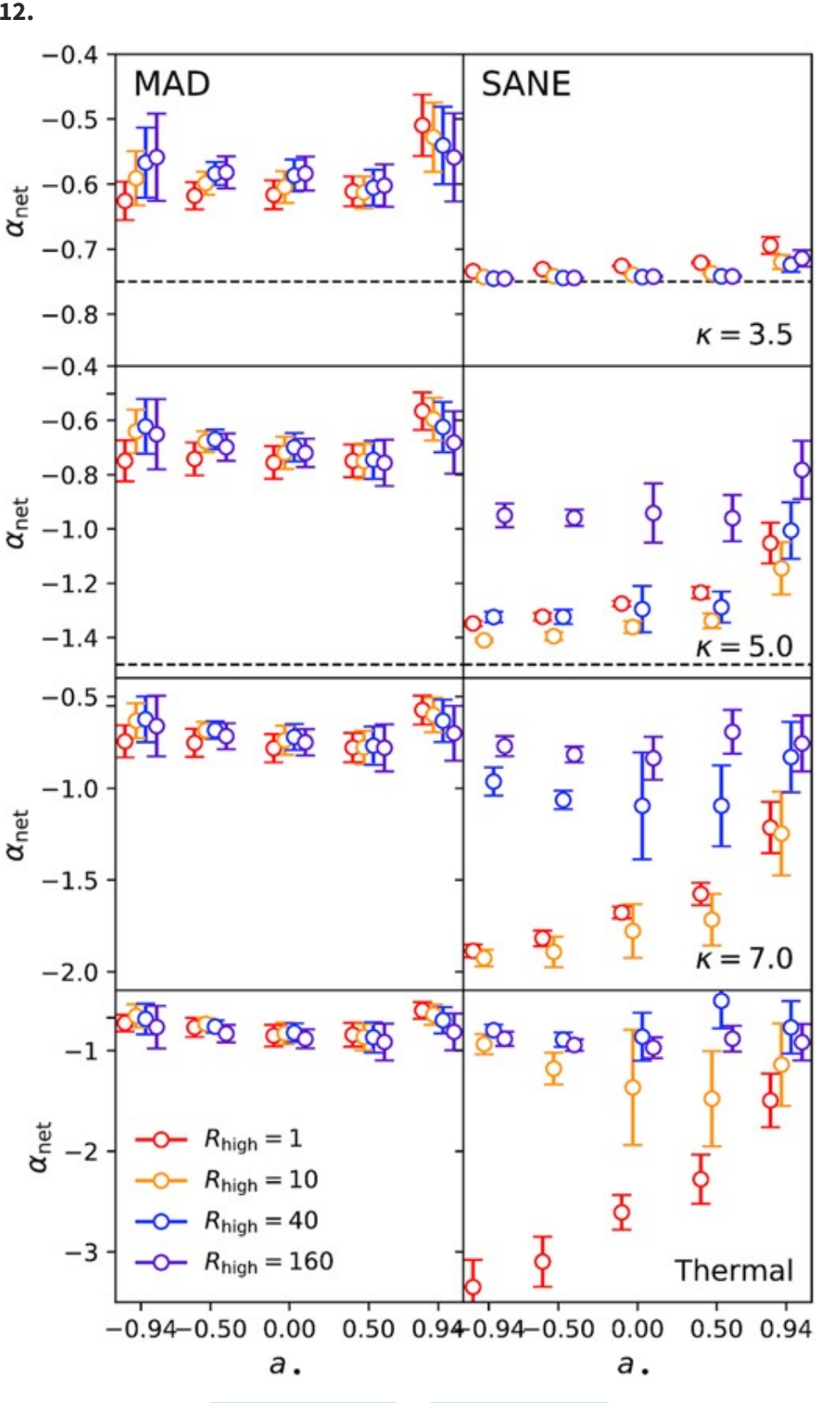

Open in new tab
Download slide

Unresolved spectral index ($\alpha_{\rm net}$, 214.1–228.1 GHz) as a function of spin for models of M87*. The left column shows MAD models, while the right column shows SANE models. From top to bottom, rows correspond to κ = 3.5, κ = 5.0, κ = 7.0, and thermal models for M87*. Different colours encode different values of $R_{\rm high}$, as indicated in the legend. Where visible, the dashed black line plots $\alpha_{\rm min}$ for a given κ. Error bars illustrate the standard deviation of $\alpha_{\rm net}$ among the 11 snapshots imaged. Most models exhibit no discernable dependence of $\alpha_{\rm net}$ on $a_\bullet$. For a given $R_{\rm high}$ and eDF, SANE models typically exhibit more negative $\alpha_{\rm net}$ than MAD models.

We repeat this analysis on our $\varkappa = 5$ models of Sgr A* in Fig. 11, now with a separate panel for each inclination studied. The same qualitative trends seen for M87* persist, although Sgr A* models tend towards larger $\langle\tau_\nu\rangle$ and therefore more positive $\alpha_{\rm net}$ than M87* models. As inclination increases, both $\langle\tau_\nu\rangle$ and $\alpha_{\rm net}$ also increase. With larger values of $\langle\tau\rangle$, the effect of $R_{\rm high}$ is more pronounced for MAD models of Sgr A* than for M87*. Our models tend to prefer more negative values of $\alpha_{\rm net}$ than the observed $\alpha = 0.0 \pm 0.1$, matched by only two MAD models with a viewing angle of 10°, but is more easily passed if the inclination is increased to 50°, by both MADs and SANEs.

To more clearly visualize differences in models as a function of spin, magnetic field state, and now also eDF, we plot for each M87* model the mean and standard deviation of $\alpha_{\rm net}$ for the 11 snapshots sampled in Fig. 12. We plot MAD models on the left column and SANE models on the right column. The different rows correspond to different eDFS, with $\varkappa = 3.5$, $\varkappa = 5.0$, $\varkappa = 7.0$, and thermal models represented from top to bottom. Different colours encode different values of $R_{\rm high}$, as indicated in the legend. Where visible, a dashed horizontal line marks $\alpha_{\rm min}$, the spectral index below which a model cannot fall given a value of $\varkappa$.

For the majority of the models, $\alpha_{\rm net}$ is generally insensitive to $a_\bullet$, which implies that $a_\bullet$ typically has little effect on B, Θ_e, and τ_ν of the emitting region. The exceptions are low $R_{\rm high}$ SANE models with large values of $\varkappa$, those SANEs which emit mostly from the disc rather than the funnel. However, these models can already be ruled out by their overly steep spectral indices, falling below even the large-scale ALMA measurement of $\alpha \approx -1.1$ (Goddi et al. 2021). Some models appear to exhibit greater magnitudes of time variability than others, likely reflecting the magnitude of $d\alpha_{\rm net}/d\tau_\nu$ for a given set of plasma parameters. In particular, the SANEs with $\varkappa = 3.5$ exhibit very little time variability, since $\alpha_{\rm net}$ is near the asymptotic value of −0.75 and insensitive to τ_ν.

For a fixed emitting region, one would expect that increasing $R_{\rm high}$ should decrease $\alpha_{\rm net}$, since the characteristic temperature of emitting electrons would decrease, causing $\nu_{\rm crit}$ to decrease. However, recall that we scale each model with different values of $\mathcal{M}$, and the emitting region does not stay the same as $R_{\rm high}$ changes (e.g. Event Horizon Telescope Collaboration 2019e). For fixed $R_{\rm high}$ and eDF, MAD models usually exhibit more positive values of $\alpha_{\rm net}$ than SANE models. This is because the weaker magnetic fields and lower temperatures of SANE models cause $\nu_{\rm crit}$ to be smaller. For $\varkappa = 3.5$, all SANE models are near $\alpha_{\rm min}$, indicating that they are in the optically thin, high-frequency limit.

4.5 230 vs 345 GHz

There are currently plans to expand the observing frequency of the EHT from 230 GHz to 345 GHz (Doeleman et al. 2019; Raymond et al. 2021). In addition to providing better spatial resolution, 345 GHz images will allow us to explore frequency-dependent signatures in two complementary bands. Here, we explore the degree to which α depends on the observing frequency by comparing α_{230} between 214.1 and 228.1 GHz and α_{345} between 340 and 350 GHz. This probes the second derivative of the flux with respect to frequency, while the spectral index probes the first. Since 230 GHz is near the maximum frequency of emission from synchrotron (e.g. Gravity Collaboration 2020; EHT MWL Science Working Group 2021), one could expect the second derivative to be significant.

We plot the spatially unresolved α_{230} versus α_{345} for our M87* models in Fig. 13, where from left-hand to right-hand panels correspond to $\varkappa$ of 3.5, 5.0, and 7.0, following the plotting scheme introduced in Fig. 10. Note the different axis limits in each panel. A dashed diagonal line marks $\alpha_{230} = \alpha_{345}$, which almost all models fall below. That is, increasing the observing frequency decreases the observed spectral index, as anticipated from Fig. 3. This occurs for two reasons. First, for a uniform parcel of gas, increasing the observing frequency decreases the optical depth, which then decreases the spectral index. Second, even in the optically thin regime, the spectral index decreases as $\nu/\nu_{\rm crit}$ increases (see Fig. 1). The frequency-dependence of α may help reconcile the flat spectral index observed by Kim et al. (2018) for M87* between 22 and 128 GHz with the more negative spectral indices our models produce at 230 GHz.

Figure 13.

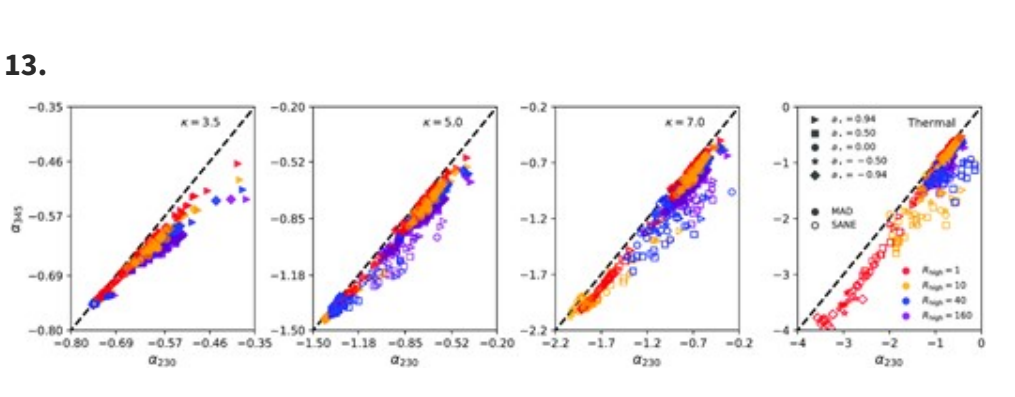

Open in new tab
Download slide

A comparison of spectral indices in the vicinity of 230 GHz (α_{230}) with those in the vicinity of 345 GHz (α_{345}). Three different values of κ are shown, 3.5, 5.0, and 7.0 from left to right. As anticipated by Fig. 3, increasing the observing frequency typically decreases the spectral index for two reasons: (i) the optical depth decreases with frequency, and (ii) $\nu/\nu_{\rm crit}$ increases with frequency, which will decrease the spectral index even in the optically thin limit (see Fig. 1).

5 DISCUSSION

5.1 Signatures in visibility amplitudes

To avoid uncertainties in image reconstruction, it may be helpful to search for signatures of spectral evolution in visibility amplitudes. Here, we define *for a fixed baseline* $\alpha_{\rm vis} = d\log|V|/d\log\nu$, where $|V|$ is the visibility amplitude. Fixing a baseline is distinct from fixing a point in the (u,v) plane, since the (u,v) distance sampled by a baseline is proportional to the observing frequency.

We find that for short baselines, those before the first null, $\alpha_{\rm vis}$ generically declines as a function of (u,v) distance. We plot three examples in Fig. 14, where a resolved spectral index map is plotted in the first column, visibility amplitudes are plotted in the second column, and $\alpha_{\rm vis}$ is plotted in the third column. From top to bottom, these plots feature models (M87* MAD $a_\bullet = -0.94$ $R_{\rm high} = 1$ thermal $i = 17°$), (Sgr A* SANE $a_\bullet = -0.94$ $R_{\rm high} = 160$ $\varkappa = 5$ $i = 90°$), and (Sgr A* SANE $a_\bullet = +0.94$ $R_{\rm high} = 40$ $\varkappa = 7$ $i = 50°$). Note that the 2017 EHT observations extended to a maximum of ≈8 Gλ. In the rightmost column, a white curve marks where the visibility amplitude drops below 1/3 of its maximum value.

Figure 14.

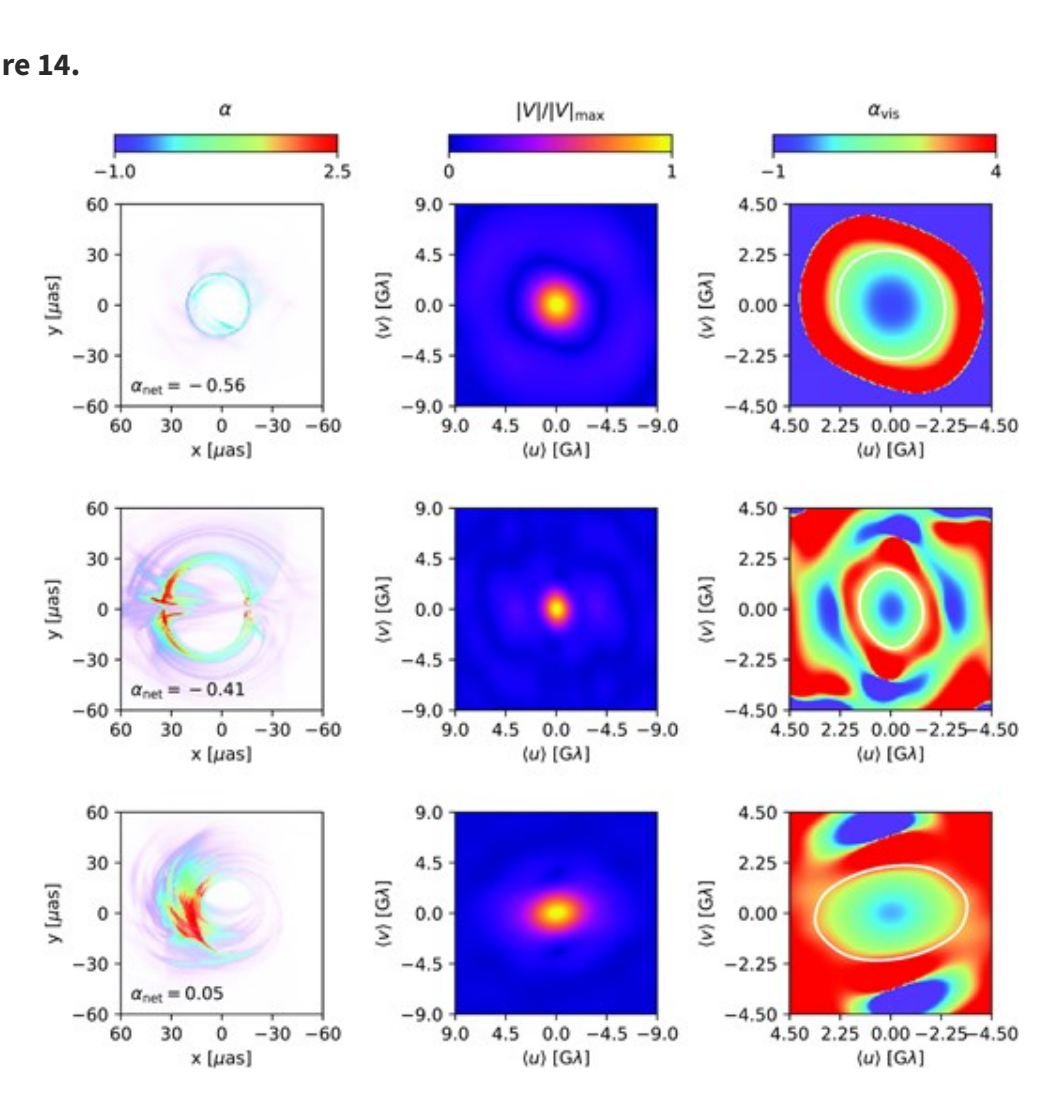

Open in new tab
Download slide

For three models, we plot their spectral index maps between 214.1 and 228.1 GHz (left), visibility amplitudes (centre) and spectral indices in visibility space (right). Models correspond to M87* MAD $a_\bullet = -0.94$ $R_{\rm high} = 1$ thermal $i = 17°$, Sgr A* SANE $a_\bullet = -0.94$ $R_{\rm high} = 160$ κ = 5 $i = 90°$, and Sgr A* SANE $a_\bullet = +0.94$ $R_{\rm high} = 40$ κ = 7 $i = 50°$. Here, $\langle u\rangle$ and $\langle v\rangle$ correspond to the *average* values of *u* and *v* between 214.1 and 228.1 GHz. That is, we keep the baselines fixed, which would otherwise move as a function of frequency. In the rightmost column, we zoom in towards the central region, marking with a white curve where the visibility amplitude drops below 1/3 of its maximum. Within this boundary, $\alpha_{\rm vis}$ increases with radius, which may be observable on the shortest EHT baselines (such as SMT-LMT; Event Horizon Telescope Collaboration 2019a). This occurs because as frequency increases, the image becomes smaller, and therefore its main peak grows larger in Fourier space.

The guiding intuition behind this trend is that α generically declines as a function of radius in real space (see Fig. 8), such that the most diffuse emission has the most negative α. As (u,v) distance increases, this diffuse emission is resolved out, resulting in a more positive $\alpha_{\rm vis}$. Beyond the central peak in Fourier space (roughly past the white contour), $\alpha_{\rm vis}$ becomes muddled, since $|V|$ is sensitive to changes in the intrinsic source structure as a function of frequency. Equivalently, Sgr A* and M87* should appear smaller with increasing frequency, which causes the main peak of its Fourier transform to grow larger. New imaging algorithms have been developed to simultaneously capture total intensity, spectral index, and even spectral curvature maps to account for these subtleties (Chael et al. 2022).

5.2 A spectral index of polarization?

Here, we briefly explore how fractional linear and circular polarization may change as a function of frequency. We define a spectral index of linear polarization $\alpha_p = d\log m/d\log\nu$ and a spectral index of circular polarization $\alpha_v = d\log|v|/d\log\nu$, where *m* and *v* are the spatially unresolved fractional linear and circular polarizations, respectively. Faraday rotation is the dominant depolarization mechanism in these models (Mościbrodzka et al. 2017; Ricarte et al. 2020; Event Horizon Telescope Collaboration 2021b), and thus the general expectation is that the linear polarization should increase as the Faraday rotation depth decreases as ν^{-2}. Meanwhile, the circular polarization fraction can exhibit many different power law dependencies on frequency depending on its origin, as discussed in detail in Wardle & Homan (2003). The circular polarization fraction should exhibit $v \propto \nu^{-1/2}$ for intrinsic emission, $v \propto \nu^{-3}$ for Faraday conversion mediated by a twist in the magnetic field, and $v \propto \nu^{-5}$ for Faraday conversion mediated by Faraday rotation. These different pathways for generating circular polarization in the context of EHT sources are discussed at length in Ricarte, Qiu & Narayan (2021).

Despite these analytic expectations, we find a surprising amount of scatter in α_p and α_v for a given eDF, with no clear patterns with respect to $R_{\rm high}$, spin, or magnetic field state (Fig. 15). We calculate α_p and α_v between 214.1 GHz and 350.0 GHz for our M87* models. We include scatter plots of these quantities in Appendix A. We do, however, notice trends as a function of eDF (Fig. 15). For each eDF, circles demarcate the 50th percentile of the distribution of these polarization spectral indices, with error bars extending to the 16th and 84th percentiles. As shown in the top panel, α_p is usually (but not always) positive. Exceptions to the rule can arise from either optical depth effects (different fractional polarizations at different optical depths) or the spatial complexity of the Faraday rotating structure[4] (Ricarte et al. 2020; Event Horizon Telescope Collaboration 2021b). Meanwhile, as plotted in the bottom panel, we find that α_v is more negative for kappa models than for thermal models. As horizontal lines, we plot analytic expectations if the circular polarization arises *solely* from a single circular polarization generation pathway. Using thermal models, Ricarte et al. (2020) showed that all three pathways are important for producing circular polarization in models of M87*. Differences in α_v may hint at a change in the dominant production pathways as a function of eDF towards Faraday conversion for kappa models instead of intrinsic emission for thermal models.

Figure 15.

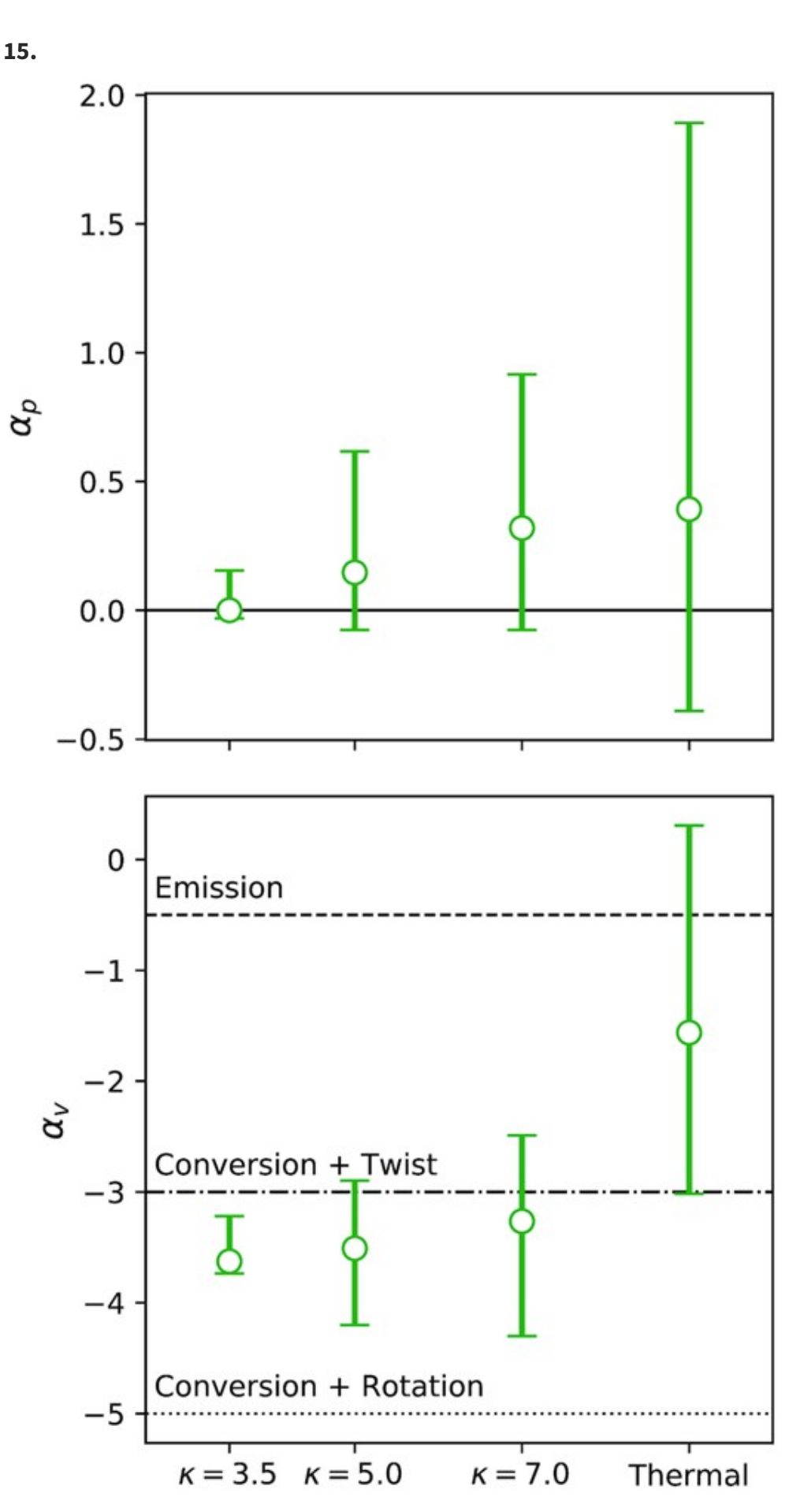

Open in new tab
Download slide

Distributions of spatially unresolved spectral indices of fractional linear polarization, α_p (top) and fractional circular polarization, α_v (bottom) between 214.1 and 350.0 GHz for models of M87*. Circles mark the median of these distributions, while errorbars span between the 16th and 84th percentiles. α_p is usually positive, consistent with decreasing Faraday depolarization at higher frequencies. Meanwhile, α_v is more negative for kappa models than thermal models, which may suggest a change in the relative importances of pathways generating circular polarization. Analytic expectations for α_v from a single zone of emission are plotted with horizontal lines.

6 CONCLUSIONS

The EHT has recently produced images of both M87* and Sgr A*, resolved on event horizon scales. This allows us to place indirect constraints on important properties of the space-time and its accretion flow, such as its spin, magnetic field state, and temperature. Spectral index information has not been included in analysis so far. On the theoretical side, predictions require at least doubling the image library across the frequency axis and are sensitive to the eDF, but are otherwise straightforward. On the observational side, a greater bandwidth is necessary to produce reliable maps in the presence of calibration errors and image reconstruction artifacts. However, spatially unresolved measurements can already place meaningful constraints on our models and help break degeneracies between parameters such as density, magnetic field strength, and temperature.

In this work, by performing GRRT calculations on a broad set of GRMHD simulations, we have studied the 230 GHz spectral index α of models of both M87* and Sgr A*. We consider both thermal and non-thermal (kappa) models of the eDF, and explore different electron temperature prescriptions as well as viewing angles for Sgr A*. Our results are summarized as follows:

i. We first establish a theoretical foundation to interpret the spectral index by studying a uniform slab of emitting plasma. Notably, the spectral index decreases as $\nu/\nu_{\rm crit}$ increases, where $\nu_{\rm crit} \propto B\Theta_e^2$. This behaviour drives most of the trends we see in our models.

ii. Consequently, α tends to be larger for MAD models than for SANE ones, since $B\Theta_e^2$ is higher for MADs than for SANEs. Since all models are scaled to produce the same 230 GHz flux, their differences in spectral index demonstrates the ability for spectral index to break model degeneracies.

iii. For resolved images, these models generically predict that α should decrease with radius, due to decreasing temperature and magnetic field strength, as well as decreasing optical depth.

iv. If resolvable by future instruments, the photon ring should exhibit a sharp peak in α, joining a chorus of polarimetric signatures: predictable shifts in the EVPA pattern (Himwich et al. 2020), linear depolarization (Jiménez-Rosales et al. 2021), and an inversion in the sign of circular polarization (Moscibrodzka, Janiuk & De Laurentis 2021; Ricarte et al. 2021).

v. Even the spatially unresolved spectral index $\alpha_{\rm net}$ varies substantially between models and can in principle be used to distinguish them. However, the exact value of $\alpha_{\rm net}$ is sensitive to the most uncertain parameters of GRRT – the electron temperature and eDF prescriptions – and should be interpreted cautiously.

vi. We show both analytically and numerically that α generically decreases with increasing frequency, due both to decreasing optical depth and increasing $\nu/\nu_{\rm crit}$.

While most EHT studies only consider thermal eDFs, we have explored the importance of the eDF in our work by studying kappa distributions, characterized by a thermal core and a non-thermal tail (Vasyliunas 1968). These distributions are motivated both observationally by the solar wind (Decker & Krimigis 2003; Pierrard & Lazar 2010) and theoretically by detailed particle-in-cell simulations (Kunz et al. 2016). Characterizing this non-thermal population has been a major uncertainty in our accretion flow models. We demonstrate a sensitivity of our images and their spectral indices to the non-thermal eDF slope, and constraining this slope will help constrain electron acceleration mechanisms. As a first step, we have only considered models in which the eDF varies globally, whereas a more physical model may allow $\varkappa$ to vary with local plasma parameters (e.g. Davelaar et al. 2018; Cruz-Osorio et al. 2022; Fromm et al. 2022; Scepi et al. 2022). We expect spectral index maps to be sensitive to these details, which would be useful to explore in future works. In addition, since the spectral index is sensitive to temperature, radiative cooling may also play a role in setting the spectral index of M87* in particular. Naively, including radiative cooling should decrease the spectral index by decreasing the temperature, but the net effect is unclear since our simulations are rescaled to match the total flux. The effect of radiative cooling is likely to only be understood satisfactorily with a different set of GRMHD simulations including such physics.

Future observations with the EHT and ngEHT with large enough bandwidth to produce spectral index maps will enable us to constrain the magnetic field strength, temperature and electron distribution of these models. At present, EHT imaging combined with multiwavelength constraints favour a spinning MAD model for M87* (Event Horizon Telescope Collaboration 2021b), and tentatively prefer the same for Sgr A*, although no model passes all constraints (Akiyama et al. 2022e). Sgr A* exhibits an unresolved spectral index of $\alpha \approx 0.0 \pm 0.1$ (Goddi et al. 2021; Wielgus et al. 2022), and our models usually predict more negative values than this (see Fig. 11). This may result in an indirect constraint on inclination that should be considered together with other constraints on Sgr A* in future work. Meanwhile, M87*'s spectral index is much more uncertain due to the unknown contribution of the large-scale jet flux, but spectral index maps will be made possible with future EHT data sets. For M87*, our MAD models of M87* tend to predict spectral indices around −0.7 regardless of spin, $R_{\rm high}$, and eDF, but SANE models produce a larger range that tends towards more negative values. SANE models of M87* with larger values of $R_{\rm high}$ tend towards more positive values of $\alpha_{\rm net}$. With resolved spectral index maps, the EHT will be able to indirectly constrain radial gradients of temperature, magnetic field strength, and density. In resolved maps, our SANE models exhibit shallower gradients with radius if there is a larger non-thermal eDF population. Under the assumption of a universal value of $\varkappa$, models are also bounded from below by $\alpha_{\rm min}(\varkappa)$ at all radii, and thus the minimum α observed places a lower limit on $\varkappa$. This information will contribute to an abundance of data about our EHT sources, which will allow us to break degeneracies and narrow even further the allowed models for these accretion flows.

ACKNOWLEDGEMENTS

We thank our anonymous referee and Alejandra Jimenez-Rosales for their thorough readings and helpful comments throughout the manuscript. We further acknowledge many fruitful and invigorating discussions with our EHT colleagues Michael Johnson, Avery Broderick, Daniel Palumbo, Zachary Gelles, and Elizabeth Himwich, George Wong, and Maciek Wielgus. This material is based upon work supported by the National Science Foundation under Grant No. OISE 1743747. This research was made possible through the support of grants from the Gordon and Betty Moore Foundation and the John Templeton Foundation. The opinions expressed in this publication are those of the author(s) and do not necessarily reflect the views of the Moore or Templeton Foundations. This work used the Frontera and Longhorn resources at Texas Advanced Computing Center through allocation AST20023.

DATA AVAILABILITY

The data underlying this article will be shared on reasonable request to the corresponding author.

Footnotes

[1] Note that we use α_ν to represent the absorptivity, but α to represent the spectral index.

[2] Throughout this work, when plotting maps of spectral index and optical depth, we linearly scale the opacity of each pixel with the total intensity in that pixel. We also saturate the opacity of the top 1 per cent of the emission to better visualize low-surface brightness material.

[3] To compute this band, we numerically compute the minimum and maximum radius of the critical curve at a viewing angle of 17° following the equations of Chael, Johnson & Lupsasca (2021).

[4] The Faraday rotator is not spatially uniform and is coincident with the emitting region. Since radiation from different emitting regions experiences different amounts of Faraday rotation on

the way to the observer, polarization which is Faraday rotated to cancel at one frequency may instead sum at another frequency.

REFERENCES

Abramowicz M. A., Chen X., Kato S., Lasota J.-P., Regev O., 1995, *ApJ*, 438, L37 10.1086/187709
Crossref Search ADS Find in my library

Akiyama K. et al. , 2022a, *ApJ*, 930, L12 10.3847/2041-8213/ac6674
Crossref Search ADS Find in my library

Akiyama K. et al. , 2022b, *ApJ*, 930, L13 10.3847/2041-8213/ac6675
Crossref Search ADS Find in my library

Akiyama K. et al. , 2022c, *ApJ*, 930, L14 10.3847/2041-8213/ac6429
Crossref Search ADS Find in my library

Akiyama K. et al. , 2022d, *ApJ*, 930, L15 10.3847/2041-8213/ac6736
Crossref Search ADS Find in my library

Akiyama K. et al. , 2022e, *ApJ*, 930, L16 10.3847/2041-8213/ac6672
Crossref Search ADS Find in my library

Akiyama K. et al. , 2022f, *ApJ*, 930, L17 10.3847/2041-8213/ac6756
Crossref Search ADS Find in my library

Bisnovatyi-Kogan G. S., Ruzmaikin A. A., 1974, *Ap&SS*, 28, 45 10.1007/BF00642237
Crossref Search ADS Find in my library

Blandford R. D., Znajek R. L., 1977, *MNRAS*, 179, 433 10.1093/mnras/179.3.433
Crossref Search ADS Find in my library

Boehle A. et al. , 2016, *ApJ*, 830, 17 10.3847/0004-637X/830/1/17
Crossref Search ADS Find in my library

Bower G. C. et al. , 2019, *ApJ*, 881, L2 10.3847/2041-8213/ab3397
Crossref Search ADS Find in my library

Chael A., Narayan R., Johnson M. D., 2019, *MNRAS*, 486, 2873 10.1093/mnras/stz988
Crossref Search ADS Find in my library

Chael A., Johnson M. D., Lupsasca A., 2021, *ApJ*, 918, 6 10.3847/1538-4357/ac09ee
Crossref Search ADS Find in my library

Chael A., Issaoun S., Pesce D. w., Johnson M. D., Ricarte A., Fromm C. M., Mizuno Y., 2022, preprint (arXiv)

Croton D. J. et al. , 2006, *MNRAS*, 365, 11 10.1111/j.1365-2966.2005.09675.x
Crossref Search ADS Find in my library

Cruz-Osorio A. et al. , 2022, *Nat. Astron.*, 6, 103 10.1038/s41550-021-01506-w
Crossref Search ADS Find in my library

Davelaar J., Mościbrodzka M., Bronzwaer T., Falcke H., 2018, *A&A*, 612, A34 10.1051/0004-6361/201732025
Crossref Search ADS Find in my library

Decker R. B., Krimigis S. M., 2003, *Adv. Space Res.*, 32, 597 10.1016/S0273-1177(03)00356-9
Crossref Search ADS Find in my library

Dexter J., 2016, *MNRAS*, 462, 115 10.1093/mnras/stw1526
Crossref Search ADS Find in my library

Doeleman S. S. et al. , 2008, *Nature*, 455, 78 10.1038/nature07245
Crossref Search ADS Find in my library PubMed

Doeleman S. et al. , 2019, *Bull. Am. Astron. Soc.*, 51, 256

EHT MWL Science Working Group, 2021, *ApJ*, 911, L11 10.3847/2041-8213/abef71
Crossref Search ADS Find in my library

Event Horizon Telescope Collaboration, 2019a, *ApJ*, 875, L1 10.3847/2041-8213/ab0ec7
Crossref Search ADS Find in my library

Event Horizon Telescope Collaboration, 2019b, *ApJ*, 875, L2 10.3847/2041-8213/ab0c96
Crossref Search ADS Find in my library

Event Horizon Telescope Collaboration, 2019c, *ApJ*, 875, L3 10.3847/2041-8213/ab0c57
Crossref Search ADS Find in my library

Event Horizon Telescope Collaboration, 2019d, *ApJ*, 875, L4 10.3847/2041-8213/ab0e85
Crossref Search ADS Find in my library

Event Horizon Telescope Collaboration, 2019e, *ApJ*, 875, L5 10.3847/2041-8213/ab0f43
Crossref Search ADS Find in my library

Event Horizon Telescope Collaboration, 2019f, *ApJ*, 875, L6 10.3847/2041-8213/ab1141
Crossref Search ADS Find in my library

Event Horizon Telescope Collaboration, 2021a, *ApJ*, 910, L12 10.3847/2041-8213/abe71d
Crossref Search ADS Find in my library

Event Horizon Telescope Collaboration, 2021b, *ApJ*, 910, L13 10.3847/2041-8213/abe4de
Crossref Search ADS Find in my library

Fishbone L. G., Moncrief V., 1976, *ApJ*, 207, 962 10.1086/154565
Crossref Search ADS Find in my library

Fromm C. M. et al. , 2022, *A&A*, 660, A107 10.1051/0004-6361/202142295
Crossref Search ADS Find in my library

Gebhardt K., Adams J., Richstone D., Lauer T. R., Faber S. M., Gültekin K., Murphy J., Tremaine S., 2011, *ApJ*, 729, 119 10.1088/0004-637X/729/2/119
Crossref Search ADS Find in my library

Goddi C. et al. , 2021, *ApJ*, 910, L14 10.3847/2041-8213/abee6a
Crossref Search ADS Find in my library

Gravity Collaboration, 2020, *A&A*, 638, A2 10.1051/0004-6361/202037717
Crossref Search ADS Find in my library

Heckman T. M., Best P. N., 2014, *ARA&A*, 52, 589 10.1146/annurev-astro-081913-035722
Crossref Search ADS Find in my library

Himwich E., Johnson M. D., Lupsasca A. r., Strominger A., 2020, *Phys. Rev. D*, 101, 084020 10.1103/PhysRevD.101.084020
Crossref Search ADS Find in my library

Howes G. G., 2010, *MNRAS*, 409, L104 10.1111/j.1745-3933.2010.00958.x
Crossref Search ADS Find in my library

Igumenshchev I. V., Narayan R., Abramowicz M. A., 2003, *ApJ*, 592, 1042 10.1086/375769
Crossref Search ADS Find in my library

Jiménez-Rosales A. et al. , 2021, *MNRAS*, 503, 4563 10.1093/mnras/stab784
Crossref Search ADS Find in my library

Kawazura Y., Barnes M., Schekochihin A. A., 2019, *Proc. Natl. Acad. Sci.*, 116, 771 10.1073/pnas.1812491116
Crossref Search ADS Find in my library

Kim J.-Y., Lee S.-S., Hodgson J. A., Algaba J.-C., Zhao G.-Y., Kino M., Byun D.-Y., Kang S., 2018, *A&A*, 610, L5 10.1051/0004-6361/201732421
Crossref Search ADS Find in my library

King A. R., Pringle J. E., Hofmann J. A., 2008, *MNRAS*, 385, 1621 10.1111/j.1365-2966.2008.12943.x
Crossref Search ADS Find in my library

Kormendy J., Ho L. C., 2013, *ARA&A*, 51, 511 10.1146/annurev-astro-082708-101811
Crossref Search ADS Find in my library

Kormendy J., Richstone D., 1995, *ARA&A*, 33, 581 10.1146/annurev.aa.33.090195.003053
Crossref Search ADS Find in my library

Kunz M. W., Stone J. M., Quataert E., 2016, *Phys. Rev. Lett.*, 117, 235101 10.1103/PhysRevLett.117.235101
Crossref Search ADS Find in my library

Mao S. A., Dexter J., Quataert E., 2017, *MNRAS*, 466, 4307 10.1093/mnras/stw3324
Crossref Search ADS Find in my library

Mizuno Y., Fromm C. M., Younsi Z., Porth O., Olivares H., Rezzolla L., 2021, *MNRAS*, 506, 741 10.1093/mnras/stab1753
Crossref Search ADS Find in my library

Mościbrodzka M., Gammie C. F., 2018, *MNRAS*, 475, 43 10.1093/mnras/stx3162
Crossref Search ADS Find in my library

Mościbrodzka M., Falcke H., Shiokawa H., 2016, *A&A*, 586, A38 10.1051/0004-6361/201526630
Crossref Search ADS Find in my library

Mościbrodzka M., Dexter J., Davelaar J., Falcke H., 2017, *MNRAS*, 468, 2214 10.1093/mnras/stx587
Crossref Search ADS Find in my library

Moscibrodzka M., Janiuk A., De Laurentis M., 2021, *MNRAS*, 508, 4282 10.1093/mnras/stab2790

Narayan R., Yi I., 1994, *ApJ*, 428, L13 10.1086/187381
Crossref Search ADS Find in my library

Narayan R., Yi I., 1995, *ApJ*, 452, 710 10.1086/176343
Crossref Search ADS Find in my library

Narayan R., Yi I., Mahadevan R., 1995, *Nature*, 374, 623 10.1038/374623a0
Crossref Search ADS Find in my library

Narayan R., Igumenshchev I. V., Abramowicz M. A., 2000, *ApJ*, 539, 798 10.1086/309268
Crossref Search ADS Find in my library

Narayan R., Igumenshchev I. V., Abramowicz M. A., 2003, *PASJ*, 55, L69 10.1093/pasj/55.6.L69
Crossref Search ADS Find in my library

Narayan R., SÄ dowski A., Penna R. F., Kulkarni A. K., 2012, *MNRAS*, 426, 3241 10.1111/j.1365-2966.2012.22002.x
Crossref Search ADS Find in my library

Özel F., Psaltis D., Narayan R., 2000, *ApJ*, 541, 234 10.1086/309396
Crossref Search ADS Find in my library

Pandya A., Zhang Z., Chandra M., Gammie C. F., 2016, *ApJ*, 822, 34 10.3847/0004-637X/822/1/34
Crossref Search ADS Find in my library

Pierrard V., Lazar M., 2010, *Sol. Phys.*, 267, 153 10.1007/s11207-010-9640-2
Crossref Search ADS Find in my library

Prather B. S., Wong G. N., Dhruv V., Ryan B. R., Dolence J. C., Ressler S. M., Gammie C. F., 2021, *J. Open Source Softw.*, 6, 3336 10.21105/joss.03336
Crossref Search ADS Find in my library

Quataert E., Gruzinov A., 2000, *ApJ*, 539, 809 10.1086/309267
Crossref Search ADS Find in my library

Raymond A. W. et al. , 2021, *ApJS*, 253, 5 10.3847/1538-3881/abc3c3
Crossref Search ADS Find in my library

Rees M. J., Begelman M. C., Blandford R. D., Phinney E. S., 1982, *Nature*, 295, 17 10.1038/295017a0
Crossref Search ADS Find in my library

Ricarte A., Prather B. S., Wong G. N., Narayan R., Gammie C., Johnson M. D., 2020, *MNRAS*, 498, 5468 10.1093/mnras/staa2692
Crossref Search ADS Find in my library

Ricarte A., Qiu R., Narayan R., 2021, *MNRAS*, 505, 523 10.1093/mnras/stab1289
Crossref Search ADS Find in my library

Rowan M. E., Sironi L., Narayan R., 2019, *ApJ*, 873, 2 10.3847/1538-4357/ab03d7
Crossref Search ADS Find in my library

Ryan B. R., Ressler S. M., Dolence J. C., Gammie C., Quataert E., 2018, *ApJ*, 864, 126 10.3847/1538-4357/aad73a
Crossref Search ADS Find in my library

Rybicki G. B., Lightman A. P., 1986, *Radiative Processes in Astrophysics*. John Wiley & Sons, Inc, New York, NY

Scepi N., Dexter J., Begelman M. C., 2022, *MNRAS*, 511, 3536 10.1093/mnras/stac337
Crossref Search ADS Find in my library

Shapiro S. L., Lightman A. P., Eardley D. M., 1976, *ApJ*, 204, 187 10.1086/154162
Crossref Search ADS Find in my library

Sądowski A., Narayan R., Penna R., Zhu Y., 2013, *MNRAS*, 436, 3856 10.1093/mnras/stt1881
Crossref Search ADS Find in my library

Vasyliunas V. M., 1968, *J. Geophys. Res.*, 73, 2839 10.1029/JA073i009p02839
Crossref Search ADS Find in my library

Volonteri M., Sikora M., Lasota J. P., Merloni A., 2013, *ApJ*, 775, 94 10.1088/0004-637X/775/2/94
Crossref Search ADS Find in my library

Wardle J. F. C., Homan D. C., 2003, *Ap&SS*, 288, 143 10.1023/B:ASTR.0000005001.80514.0c
Crossref Search ADS Find in my library

Wielgus M. et al. , 2020, *ApJ*, 901, 67 10.3847/1538-4357/abac0d
Crossref Search ADS Find in my library

Wielgus M. et al. , 2022, *ApJ*, 930, L19 10.3847/2041-8213/ac6428
Crossref Search ADS Find in my library

Wong G. N. et al. , 2022, *ApJS*, 259, 64 10.3847/1538-4365/ac582e
Crossref Search ADS Find in my library

Xiao F., 2006, *Plasma Phys. Control. Fusion*, 48, 203 10.1088/0741-3335/48/2/003
Crossref Search ADS Find in my library

Yuan F., Narayan R., 2014, *ARA&A*, 52, 529 10.1146/annurev-astro-082812-141003
Crossref Search ADS Find in my library

APPENDIX A: COMPLETE SCATTER PLOTS OF POLARIZATION SPECTRAL INDICES

In Section 5.2, we explore polarization spectral indices α_p and α_v, how rapidly the fractional linear and circular polarization change as a function of frequency. We plotted broad trends as a function of eDF in Fig. 15. Now in Fig. A1, we provide full scatter plots of α_p and α_v for our M87* models between 214.1 and 350.0 GHz, using the plotting scheme introduced in Fig. 10. Note the different extents of both axes in each panel. We do not find any significant trends in these quantities as a function of spin, magnetic field state, or R_{high}. However, each eDF does cluster in a different region, as plotted in Fig. 10.

Figure A1.

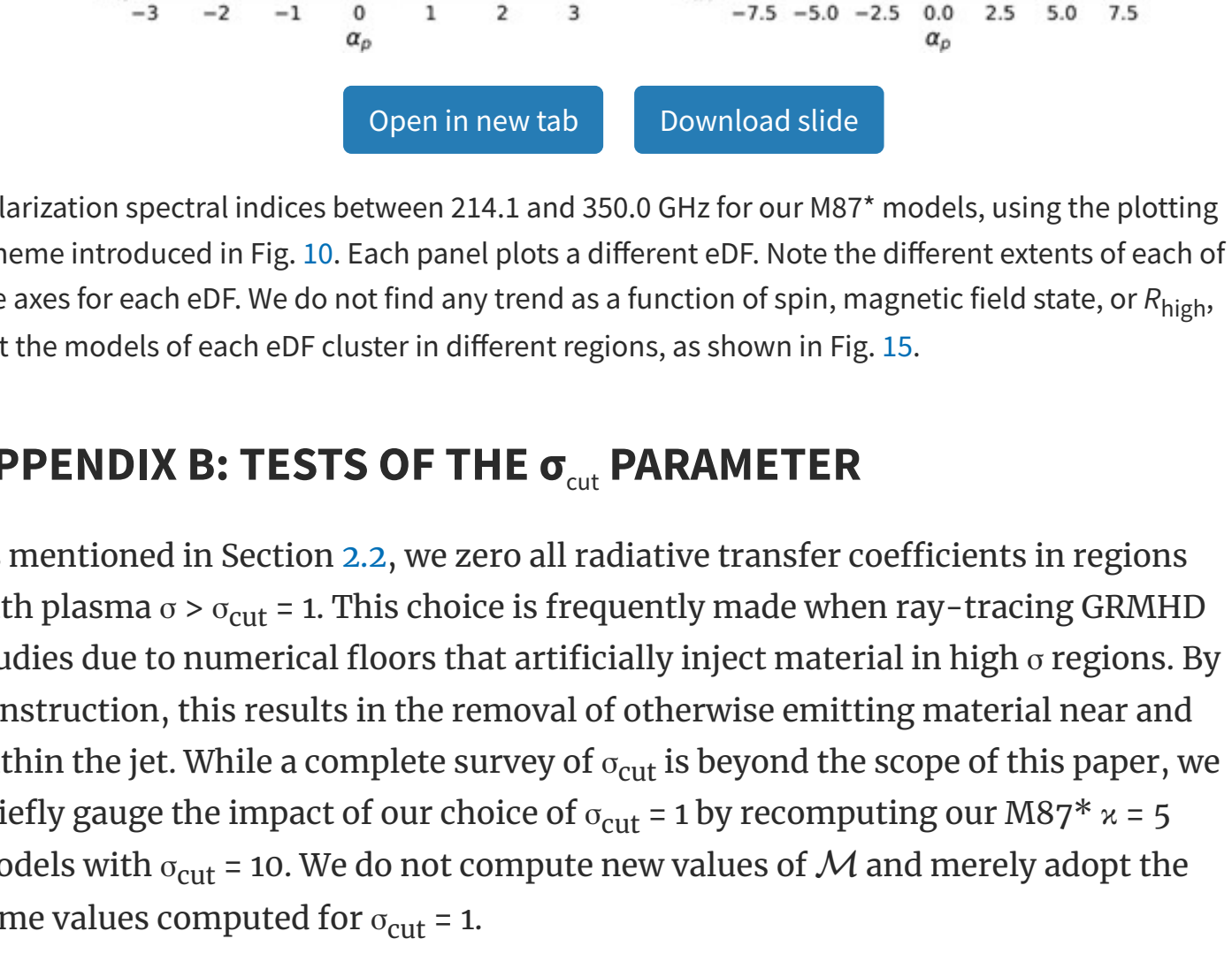

Open in new tab Download slide

Polarization spectral indices between 214.1 and 350.0 GHz for our M87* models, using the plotting scheme introduced in Fig. 10. Each panel plots a different eDF. Note the different extents of each of the axes for each eDF. We do not find any trend as a function of spin, magnetic field state, or R_{high}, but the models of each eDF cluster in different regions, as shown in Fig. 15.

APPENDIX B: TESTS OF THE σ_{cut} PARAMETER

As mentioned in Section 2.2, we zero all radiative transfer coefficients in regions with plasma $\sigma > \sigma_{\mathrm{cut}} = 1$. This choice is frequently made when ray-tracing GRMHD studies due to numerical floors that artificially inject material in high σ regions. By construction, this results in the removal of otherwise emitting material near and within the jet. While a complete survey of σ_{cut} is beyond the scope of this paper, we briefly gauge the impact of our choice of $\sigma_{\mathrm{cut}} = 1$ by recomputing our M87* ϰ = 5 models with $\sigma_{\mathrm{cut}} = 10$. We do not compute new values of $\mathcal{M}$ and merely adopt the same values computed for $\sigma_{\mathrm{cut}} = 1$.

A comparison of $\sigma_{\mathrm{cut}} = 1$ and $\sigma_{\mathrm{cut}} = 10$ models in the style of Fig. 12 is shown in Fig. B1. While the general trends remain the same, the spectral index tends to become more positive with $\sigma_{\mathrm{cut}} = 10$. This is because more material is allowed to contribute to the emission, increasing the optical depth, and this additional emission also originates from hot magnetized regions. Larger differences are seen for models with larger values of R_{high}, which have larger $\mathcal{M}$. Models where ϰ varies based on local plasma properties (e.g. Davelaar et al. 2018; Fromm et al. 2022; Scepi et al. 2022) are likely to be more sensitive to the choice of σ_{cut}.

Figure B1.

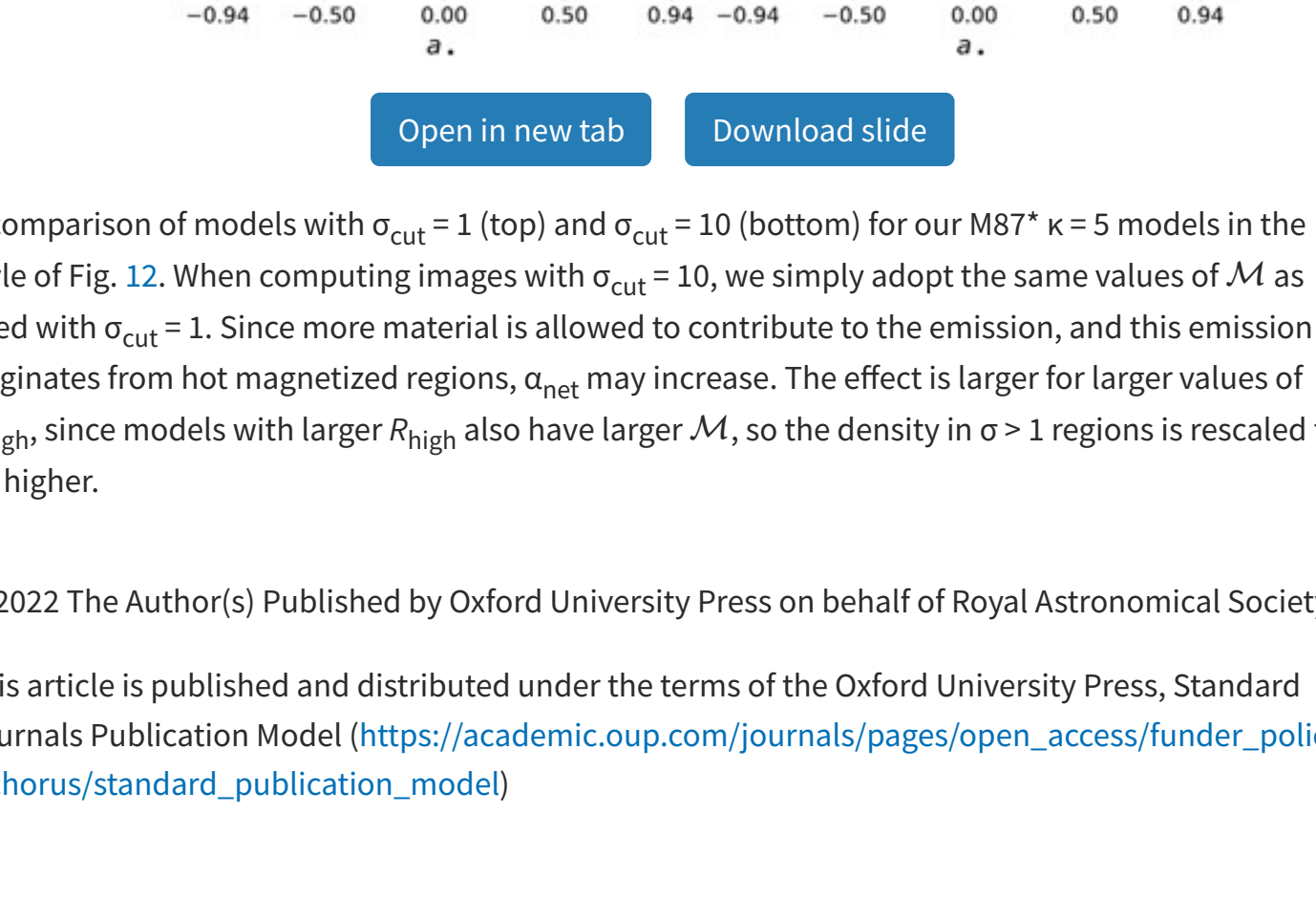

Open in new tab Download slide

A comparison of models with $\sigma_{\mathrm{cut}} = 1$ (top) and $\sigma_{\mathrm{cut}} = 10$ (bottom) for our M87* κ = 5 models in the style of Fig. 12. When computing images with $\sigma_{\mathrm{cut}} = 10$, we simply adopt the same values of $\mathcal{M}$ as used with $\sigma_{\mathrm{cut}} = 1$. Since more material is allowed to contribute to the emission, and this emission originates from hot magnetized regions, α_{net} may increase. The effect is larger for larger values of R_{high}, since models with larger R_{high} also have larger $\mathcal{M}$, so the density in σ > 1 regions is rescaled to be higher.

© 2022 The Author(s) Published by Oxford University Press on behalf of Royal Astronomical Society

This article is published and distributed under the terms of the Oxford University Press, Standard Journals Publication Model (https://academic.oup.com/journals/pages/open_access/funder_policies/chorus/standard_publication_model)

Monthly Notices of the Royal Astronomical Society
COMETS SPECIAL ISSUE
A New Vision After Rosetta and Philae
FREELY AVAILABLE ONLINE

Online ISSN 1365-2966 Print ISSN 0035-8711 Copyright © 2024 The Royal Astronomical Society

Oxford University Press is a department of the University of Oxford. It furthers the University's objective of excellence in research, scholarship, and education by publishing worldwide

Oxford University Press uses cookies to enhance your experience on our website. By selecting 'accept all' you are agreeing to our use of cookies. You can change your cookie settings at any time. More information can be found in our Cookie Policy.

Accept all Cookie settings